

POLITECNICO DI TORINO



Master of Science in Aerospace and Astronautical
Engineering

Master Thesis

Experimental study of a Resonance Igniter for space propulsion applications

Supervisor

Prof. Dario Pastrone

Co-supervisors

Ing. Andrea Ferrero

Ing. Antonietta Conte

Ing. Filippo Masseni

Candidate

Davide Difrancesco

April 2020

Abstract

The research, conducted towards designing a new and reliable ignition method for rocket engines, has influenced over the years the design of rocket combustion chambers. This thesis work has the purpose of simulating the phenomena related to resonance heating processes, by means of an experimental facility designed to conduct tests and looking for the best setup in order to reproduce the resonance ignition phenomenon.

A resonance igniter takes advantage of a gasdynamic phenomena called resonance heating which occurs inside it, heating up the propellant beyond its auto-ignition temperature. This ignition method has increased its importance in rocket engines field due to its reliability and its relative simplicity of construction. The main features of the facility are based both on previous studies conducted by TUM (Technische Universität of München) and experimental tests carried out during the present work. Tests have been conducted using different experimental configurations, first focusing only on the validation of the resonance heating phenomenon and subsequently aiming to obtain more accurate results through some gradual upgrades on the entire facility.

The thesis can be divided into three main parts. In the first part a theoretical approach to the phenomenon is introduced, describing the influence of its driven parameters besides analyzing the physical processes lying behind resonance heating processes. The core part offers a global view on both the experimental facility designed for the tests and improved later, and the experimental results coming from the performed test campaign. The latter has been conducted using two different configurations of the apparatus and parameter values. Final considerations about the experimental tests results, along with possible future perspectives of resonance ignition method are discussed in the last part of the thesis.

Contents

1	Resonance ignition fundamentals	1
1.1	Introduction	1
1.2	General description of resonance heating	2
1.3	Theoretical approach	5
1.3.1	Shock tube theory	5
1.3.2	H-S tube model	7
1.4	Resonator thermal processes	10
1.4.1	Heating production mechanisms	10
1.4.2	Heating removal mechanisms	13
1.4.3	Power thermal balance	15
1.5	Resonance igniter operating modes	17
1.6	Driven parameters of resonance heating	20
1.6.1	Nozzle Pressure / NPR	20
1.6.2	Nozzle-cavity distance	20
1.6.3	Cavity depth	24
1.6.4	Cavity shape	25
1.6.5	Resonator materials	26
1.6.6	Gas composition	30
1.6.7	Other parameters	32
2	Experimental apparatus	34
2.1	Preliminary setup considerations	34
2.2	Description of components	35
2.2.1	Resonator configurations	35
2.2.2	Thermocouple	38
2.2.3	Pressure transducer	41
2.2.4	Microphone	43

2.2.5	Compressed air line	44
2.3	Data acquisition and processing	46
2.3.1	Hardware section	46
2.3.2	Software section	51
2.4	Global facility setup	54
2.4.1	Initial tests setup	54
2.4.2	Final facility setup	57
3	Test Campaign	59
3.1	First validation tests	59
3.2	Final validation tests	62
4	Conclusions	68
4.1	Discussion of results	68
4.2	Future perspectives	69

List of Figures

1.1	<i>Nozzle and resonator included in resonant igniter apparatus [4]</i>	3
1.2	<i>Under-expanded nozzle jet flow (bottom), with instability region (top), from the first Hartmann experiment about acoustic waves generation [20]</i>	3
1.3	<i>Simplified distance-time graphic of oscillation process inside HS tube [9]</i>	4
1.4	<i>Initial conditions inside the shock tube [6]</i>	5
1.5	<i>Shock tube flow [13]</i>	6
1.6	<i>Shock tube after shock wave reflection [6]</i>	7
1.7	<i>Formation of stagnant section inside shock tube [6]</i>	8
1.8	<i>Gas flow evolution represented on temperature-entropy diagram [12]</i>	11
1.9	<i>Time-distance diagram of cavity flow relative to a single cycle, with the various flow zones indicated [12]</i>	12
1.10	<i>Influence of Mach number on penetration length L_p of the nozzle jet flow [12]</i>	14
1.11	<i>Variation of ϕ functions related to Mach number M_2, for air at ratio $L/D = 33$ [12]</i>	16
1.12	<i>First shock location related to nozzle pressure ratio, for different nozzle-cavity distances [29]</i>	18
1.13	<i>Influence of nozzle pressure on pressure waves amplitude, for different NPR values (brass conical cavity, nitrogen, nozzle-cavity gap: 0,45 inch) [27]</i>	21
1.14	<i>Influence of NPR on endwall temperature, for different nozzle pressure values (brass conical cavity, nitrogen) [27]</i>	21
1.15	<i>Dimensionless pressure at the jet centerline as a function of dimensionless nozzle-resonator distance [15]</i>	22

1.16	<i>Position of first cell boundary and inlet cavity position related to peak endwall temperature, for different NPR values</i>	23
1.17	<i>Cavity endwall temperature variation related to nozzle-cavity distance, for different values of nozzle pressure [27]</i>	23
1.18	<i>Cavity endwall pressure waves amplitude (top) and period variation (bottom) related to different values of cavity depth [27]</i>	24
1.19	<i>Variation of cavity endwall temperature related to nozzle pressure, for different values of resonator depth [27]</i>	25
1.20	<i>Influence of resonator shape on endwall temperature, for different nozzle pressure values [27]</i>	26
1.21	<i>Differences in endwall temperature between standard and extended tapered resonator configurations [27]</i>	27
1.22	<i>Temperatures reached with tapered (conical) and 3-steps resonators (NPR=4) [8]</i>	27
1.23	<i>Temperatures on resonator cavity endwall related to nozzle-cavity distance / nozzle diameter ratio (L/D), for different materials [9]</i>	28
1.24	<i>Influence of materials and tube walls thickness on temperature along a cylindrical cavity (Helium, jet flow Mach=0.96) [12]</i>	29
1.25	<i>Temperature variation along two square-section cavity made of wood and iron (Air, jet flow Mach=0.84) [12]</i>	30
1.26	<i>Influence of gas composition (H_2, N_2) on cavity endwall temperature, related to nozzle pressure (NPR=4.5, nozzle-cavity gap=0.45 inch) [27]</i>	31
1.27	<i>Influence of different gases on cavity endwall temperature, for different nozzle-cavity gaps (from left to right: Helium, Argon, Nitrogen; stepped-cavity, $p_n=7$ bar) [9]</i>	31
1.28	<i>Influence of nozzle jet flow Mach number on temperature along the cavity [12]</i>	33
1.29	<i>Differences on achieved temperature along the cavity, for resonator with and without thermal insulation [12]</i>	33
2.1	<i>Cavity configurations: 3-steps (above), conical (below) [8]</i>	35
2.2	<i>2-D drawing of both 3-step resonators (wood, PMMA) used for validation tests</i>	36

2.3	<i>PMMA resonator used for validation tests</i>	36
2.4	<i>3-D model of conical resonator (final configuration) used for final tests</i>	37
2.5	<i>2-D drawing of conical resonator (final configuration) with dimensions</i>	37
2.6	<i>Safety factor (FOS) derived from stress analysis on conical resonator</i>	38
2.7	<i>Basic scheme of a thermocouple [30]</i>	39
2.8	<i>Temperature ranges and output voltages for different types of thermocouples [21]</i>	40
2.9	<i>Different configuration of thermocouples sheathing [21]</i>	40
2.10	<i>Wika[®] A-10 pressure transducer</i>	42
2.11	<i>Dimensions and internal detail with electrical connections</i>	42
2.12	<i>Microphone used for amplitude and frequency measurements</i>	43
2.13	<i>Compressors used on the experimental tests</i>	44
2.14	<i>Compressed air tank</i>	45
2.15	<i>NI Field Point modules</i>	46
2.16	<i>Basic scheme and dimensions of NI[®] cFP-1804 with back-plane slots</i>	47
2.17	<i>Thermocouple connection scheme for NI[®] cFP-TC-120 module [3]</i>	48
2.18	<i>Electrical scheme for current source connection to NI[®] cFP-AI-100 [2]</i>	48
2.19	<i>Internal screw-terminal arrangement for NI[®] cFP-CB-3 connector block [1]</i>	49
2.20	<i>Internal screw-terminal arrangement for NI[®] cFP-CB-1 connector block [1]</i>	50
2.21	<i>Pressure transducer and cFP modules electrical connection diagram</i>	50
2.22	<i>LabVIEW[®] script used for acquisition and processing of temperature signals from the thermocouple</i>	52
2.23	<i>LabVIEW[®] script used for acquisition and processing of pressure waves amplitude and frequency signals from the microphone</i>	52
2.24	<i>LabVIEW[®] script used for acquisition and processing of pressure levels read by pressure transducer</i>	53
2.25	<i>Wood block with cavity hole used for first validation tests</i>	54

2.26	Wood 3-step cavity dimensions	55
2.27	Compressor and tank set up for validation tests	56
2.28	Nozzle and PMMA resonator configuration for validation tests	56
2.29	Scheme of validation tests facility	56
2.30	Final facility configuration	57
2.31	Micrometric positioning sliding	58
2.32	Scheme of upgraded facility	58
3.1	Experimental test example performed with wood cavity . . .	59
3.2	Second tests series temperature graphic	61
3.3	Maximum temperature reached during final validation tests (Test #3	63
3.4	Pressure waves amplitude and frequency spectrum correspond- ing to the test #3	64
3.5	Pressure waves amplitude and frequency spectrum for test #1	65
3.6	Pressure waves amplitude and frequency spectrum for test #2	66
3.7	Frequency spectrum and amplitude of tests #1,#2,#3, with first three resonator cavity longitudinal frequencies	66

List of Tables

2.1	<i>Wika[®] A-10 pressure transducers specifications</i>	41
2.2	<i>Pressure transducer main specifications</i>	42
2.3	<i>Microphone main specifications</i>	43
2.4	<i>Compressors main specifications</i>	45
2.5	<i>Data acquisition modules main specifications [3],[2]</i>	48
2.6	<i>cFP-AI-100 channels associated to cFP-CB-1 terminals [2]</i>	51
3.1	<i>First test series results with PMMA resonator</i>	60
3.2	<i>Second test series results with PMMA resonator</i>	61
3.3	<i>Final validation tests results</i>	63

Chapter 1

Resonance ignition fundamentals

1.1 Introduction

The phenomenon of resonance heating has been the subject of many experimental and analytical effort over the years [27], starting from 1922 when Hartmann investigated convergent nozzles directing underexpanded flows at cavities closed at one end[20]. He discovered this system was unstable producing intense high-frequency noise [8]. Later, the work of Sprenger in 1954 showed that pressure oscillations inside a cylindrical cavity were accompanied by an intense heat release at the bottom of it. The temperature here could be several times higher than the gas jet stagnation temperature depending on design characteristics [31].

These observations and other experiments conducted in the following years and on recent times have increased the interest of resonance heating in the field of rocket engines, because of its capability in achieving the ignition of liquid propellant engines. The high reliability and safety of the electrical ignition method for liquid-propellant rocket engines has been proven [16]. However, it requires an electrical source of power to work. On the other hand, resonant igniters are lightweight, highly reliable and do not need an electrical source and movable parts to work [15]. Therefore, resonance ignition could substitute the classical electrical spark ignition method, besides being an advantage especially for those space missions which require multiple re-ignitions. Investigations about resonance heating mechanism have been

carried on considering the dependence of this phenomenon on some driven parameters such as *nozzle-resonance cavity opening distance*, *nozzle diameter*, *nozzle pressure ratio*, in addition to the complexity of flow structure of the underexpanded gas jet [24].

In order to understand how a resonance igniter works it is necessary to consider the principles of resonance heating phenomenon which takes place into it. Therefore, the influence of driven parameters of resonance ignition process will be analyzed in the next sections, along with a theoretical explanation of what happens inside the resonance tube.

1.2 General description of resonance heating

Resonance heating process starts when an under-expanded gas jet comes out from a *nozzle* and enters inside a cavity closed at one end (*resonator*). The latter is generally called *Hartmann-Sprenger tube* after the discoveries regarding resonance heating phenomenon made by Hartmann in 1922 and Sprenger in 1954. Nozzle and resonator are therefore the two main and essential components which constitute a resonance igniter.

In the space between them (indicated as *gap distance*, on *Figure 1.1*), considering a sonic nozzle, the typical "*barrel*" structure of an under-expanded jet will form with compression and expansion zones. This originates from the interaction between incident, reflected shocks and the Mach disk, in addition to a detached bow shock placed at the cavity inlet. The bow shock starts to oscillate leading to the resonance phenomenon, when the resonator is placed in the so-called regions of *instability* [15]. These regions are unstable zones of the flow where the pressure rises until reaching a peak, as seen on top of *Figure 1.2* (intervals a_1b_1 , a_2b_2 , a_3b_3). Compression waves detach from the oscillating bow shock, are reflected from the cavity endwall, then travel backwards the tube inlet coupling with and reinforcing the bow shock [27]. This process, schematically depicted on bottom of *Figure 1.2*, will continue to be repeated many other times producing a series of flow oscillations. As a consequence of these fluctuations, it has been demonstrated that the gas inside the cavity can be heated up reaching temperatures from 500-700 K [19, 31], up to 1600 K or more [25].

The time-distance graphic in *Figure 1.3* shows the process briefly described above. The dashed line represents the contact surface between the driving

1.2. General description of resonance heating

jet flow and the indigenous gas inside the HS tube, while the continuous line indicates the path of the shock wave generated after the coalescence of compression waves detached from the bow shock.

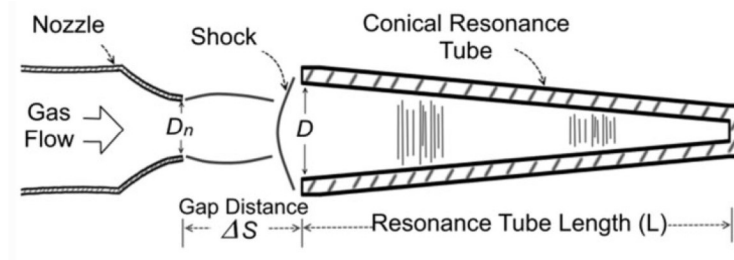


Figure 1.1: Nozzle and resonator included in resonant igniter apparatus [4]

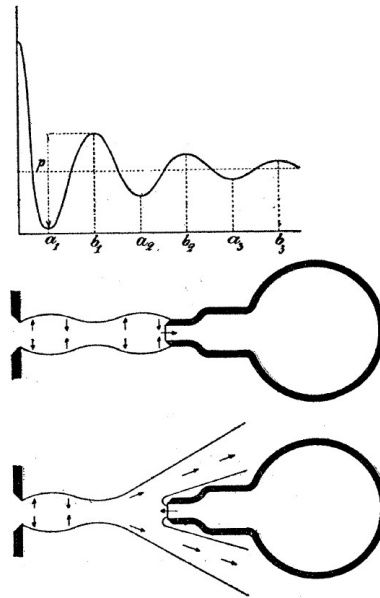


Figure 1.2: Under-expanded nozzle jet flow (bottom), with instability region (top), from the first Hartmann experiment about acoustic waves generation [20]

As described by Brocher and Ardissonne [9], initially the jet flow enters inside the cavity while producing a shock wave which is reflected at the closed end. The reflected shock wave travels back towards the cavity inlet and pushes the driving jet sideways. At this point the tube begins its emptying phase, with an expansion wave which enters the tube, is reflected at the endwall, and travels upstream. When this expansion wave reaches the cavity inlet

the driving jet flow is sucked again into the tube, so a new cycle can begin. The driving jet flow coming out from the nozzle can penetrate up to a certain length inside the resonance tube, indicated on the graphic below as the penetrating length of driving gas. This distance will increase with the Mach number of the jet [9].

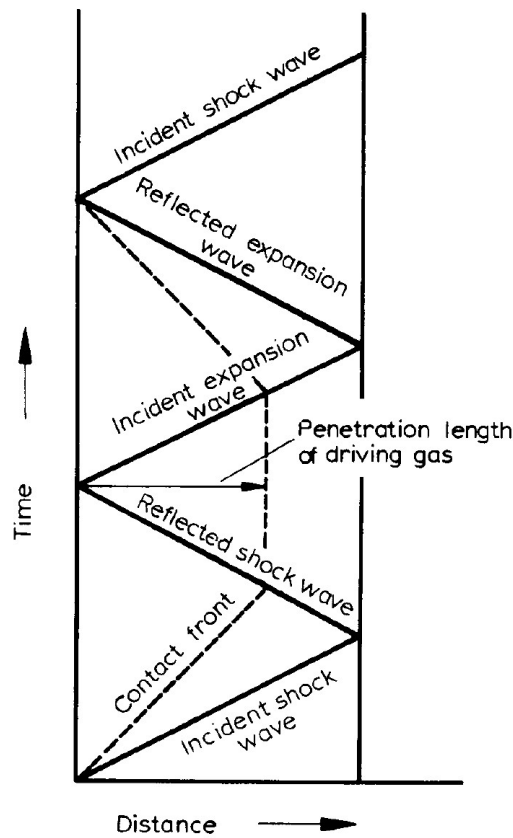


Figure 1.3: *Simplified distance-time graphic of oscillation process inside HS tube [9]*

1.3 Theoretical approach

This section is dedicated to the theory lying behind the resonance ignition phenomenon, from shock tube model to the description of heating process mechanisms occurring inside the resonator cavity.

1.3.1 Shock tube theory

The resonator tube bases its functioning on a similar device called *shock tube*, as defined in fluid dynamics literature [6]. Shock tube is a tube closed at both end, where compression waves cyclically propagate inside it and are reflected from one of the two closed wall, creating an unsteady wave motion. This situation can be represented by means of gasdynamic relations regarding the propagation of shock waves into a cavity. The initial conditions inside the shock tube are depicted on *Figure 1.4*. A diaphragm separates the high pressure section, which represents the free jet flow in the case of H-S tube, from the low pressure zone which is similar to the pressure condition into the resonator. In general the two zones can contain two different gas species, but in this case of study the gas is the same on both sections.

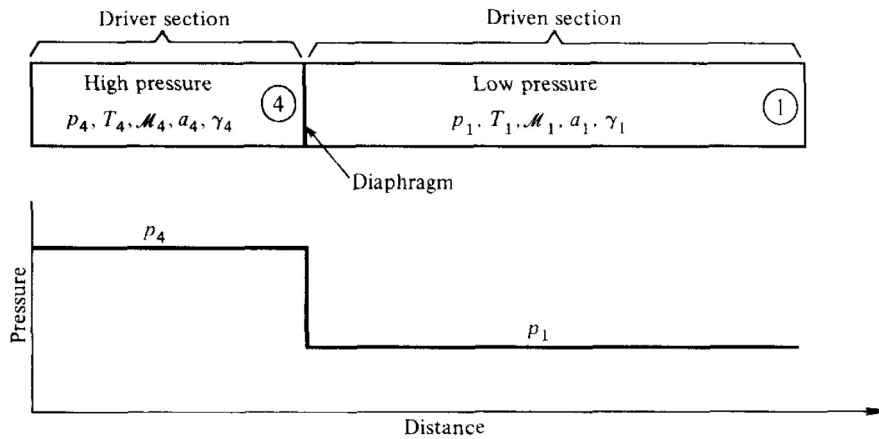


Figure 1.4: *Initial conditions inside the shock tube* [6]

When the diaphragm breaks ($t = 0$), the high pressure gas rushes into the low pressure region. Pressure waves propagate into the latter (*driven section, 1*), coalescing and forming a shock wave, while expansion waves propagate into high pressure section (*driver section, 4*). Shock wave forms because of

a non-linear steepening process, due to the fact that the speed of a pressure wave increases while increasing the temperature [13]. As it can be seen from the situation shown on *Figure 1.5*, this has some effects on pressure, temperature and velocity:

- the *pressure* behind the shock rises, tending to uniform to the maximum value of the high pressure region (p_4);
- the *temperature* of the region between the shock wave and the contact surface increases, while the region occupied by the expansion waves gets colder compared with initial conditions (T_4);
- this pressure rise induces a gas mass motion with *velocity* (u_p), equal to the velocity of the contact surface (dash line) [6].

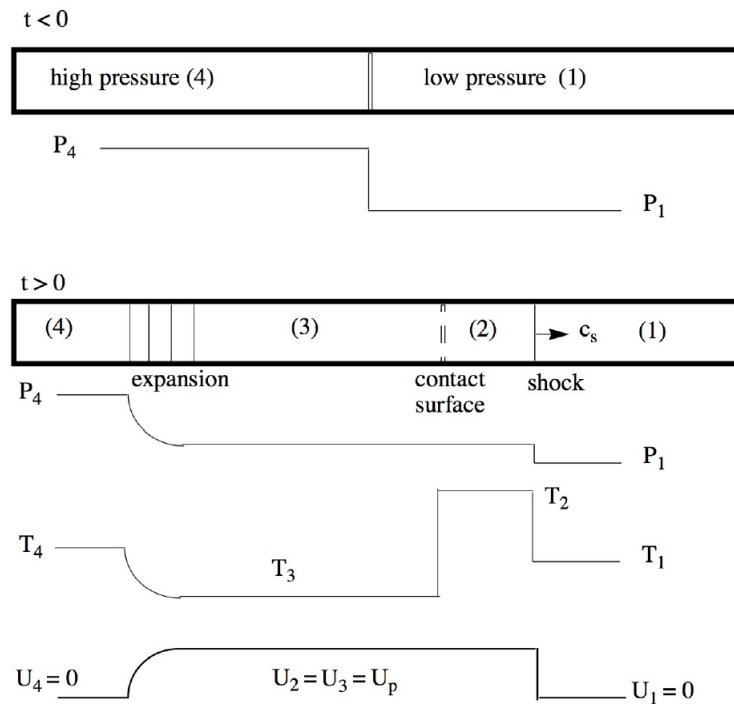


Figure 1.5: *Shock tube flow* [13]

The *contact surface* represents the interface between the two regions of shock tube, which act as a piston producing a shock wave moving at a speed equal to c_s [13]. Through this surface, pressure and gas flow speed remain constant

($p_3 = p_2$, $u_3 = u_2 = u_p$). In this first phase the normal shock wave travels towards one end of the tube with a speed equal to c_s , while expansion waves propagate in the opposite direction.

Subsequently, the shock wave impinges on the tube endwall where it was heading to. As a natural response to this, a normal shock wave is generated in the opposite direction as seen in *Figure 1.6* [6]. Behind the reflected shock wave (*section 5*) the gas stands still, while the first moves towards the gas flow with such velocity to stop the gas mass motion (*section 2*).

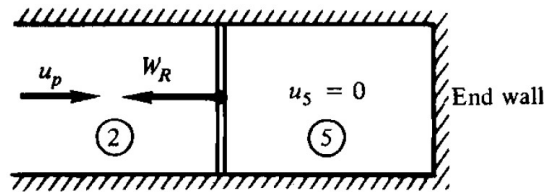


Figure 1.6: Shock tube after shock wave reflection [6]

1.3.2 H-S tube model

The main difference between the shock tube previously analyzed and the Hartmann-Sprenger tube, which is the subject of the present work, lies into their different geometry. In particular, the opening on one of the tube endwall, in H-S tube, allows the jet stream from the nozzle to enter inside the cavity cycle after cycle so that pressure oscillations can be achieved establishing the necessary conditions for resonance heating. It can be said as well that if the shock in the inflow phase is strong enough, the gas flow exits from the resonator as an underexpanded jet colliding with the upstream free jet which comes out from the nozzle. The reflected shock wave, on the other hand, travels towards the cavity opening until it is reflected again as an expansion wave [7]. As regards the nozzle-resonator system, a theoretical model was proposed from Kessaev in 1990 [23] and reported also by Danton, Villas Boas and Niwa [18]. It asserts that the reflected shock wave interacts with the gas still entering inside the cavity and creates a section where the gas remains stagnant, as shown on *Figure 1.7*. This section of the resonator, placed near its closed endwall, contains the gas compressed and heated on every cycle which can permit the ignition of the propellant after reaching the auto-ignition temperature of the latter. Moreover, the gas flow entering

during the cycles will not penetrate this stagnant section allowing the temperature to rise up [18].

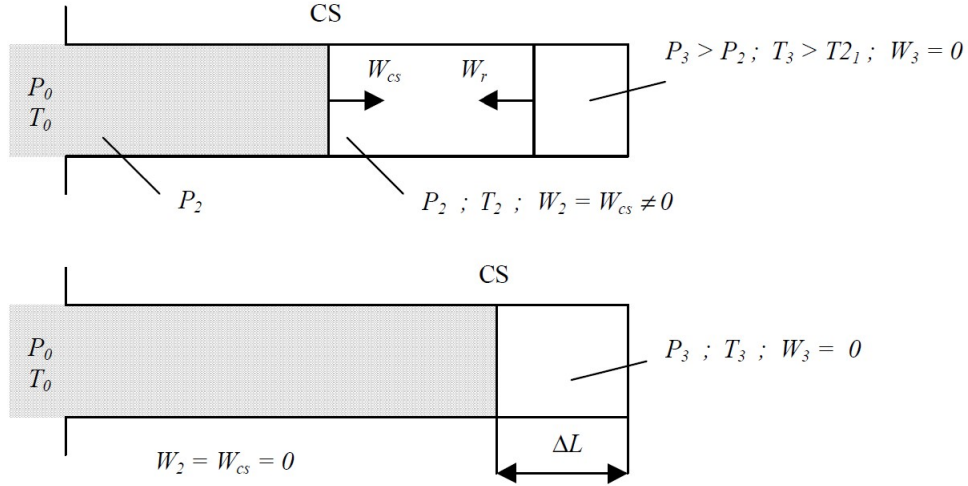


Figure 1.7: Formation of stagnant section inside shock tube [6]

Apart from the detailed theory for the description of resonance heating, some easier theoretical considerations could be done though, considering for example the theoretical approach of Sarohia, Back et al. [29]. Consequently, a way to determine the absolute pressure levels inside the tube can be obtained from the following relation [29]:

$$\frac{p_3 - p_2}{p_2 - p_1} = \frac{\frac{2\gamma}{\gamma+1} \left(\frac{p_2}{p_1}\right)}{1 + \frac{\gamma-1}{\gamma+1} \left(\frac{p_2}{p_1}\right)}$$

where γ indicates the specific heat ratio of the gas.

From the previous equation, knowing the jump across the incident shock wave ($p_3 - p_2$) and reflected shock wave ($p_2 - p_1$), it is possible to determine the pressure ratio across the incident wave ($\frac{p_2}{p_1}$), as well as pressures p_3 , p_2 and p_1 . The Mach number of the incident shock wave (M_s) can be determined from the relation [29]:

$$M_s^2 = 1 + \left(\frac{\gamma+1}{2\gamma}\right) \left(\frac{p_2}{p_1} - 1\right)$$

The speed of contact surface behind the incident shock wave (U_c) and the speed of the latter (U_s) are related through the following equation [29]:

$$\frac{U_c}{U_s} = \frac{\frac{2}{\gamma+1} \left(\frac{p_2}{p_1} - 1 \right)}{\left(\frac{p_2}{p_1} \right) + \frac{\gamma-1}{\gamma+1}}$$

, while the relation between the speed of reflected shock wave (U_r) and that of the incident wave could be written, after some substitutions, as follows [29]:

$$\frac{U_r}{U_s} = 1 - \left(\frac{3-\gamma}{2} \right) \frac{U_c}{U_s}$$

The previous relations show how the ratio between reflected and incident shock wave velocities depends only on the specific heat ratio of the gas, while for contact surface and incident shock wave velocities ratio there is also a dependency from pressure ratio ($\frac{p_2}{p_1}$) [29].

1.4 Resonator thermal processes

The exact study of thermal effects occurring in Hartmann-Sprenger tubes is not an easy matter, especially because of the unsteady nature of the flow inside the cavity and the presence of discontinuity surfaces such as shock waves and the contact surface. However, from the studies of Kawahashi and Suzuki [22], the basic relations which can be used to characterize and study the resonance heating phenomenon are the conservation equations (continuity, momentum, energy transport) besides entropy conservation equation and second law of thermodynamic for the determination of gas temperature. Main assumptions must be those of a one-dimensional unsteady flow and the presence of wall friction and heat transfer [22], which are crucial for the definition of the heating process inside the resonator. As regards the heating mechanisms, Sarohia and Back imputed to the irreversible processes occurring across the compression wave fronts the main cause of the intense heating shown by the gas trapped at cavity base [28]. However, it is more accurate to mention all the heating mechanisms involved in this complex process dividing them into those which are responsible for the increase of temperature at the cavity base, and those related to heating removal from the cavity itself. Basically they are :

- *dissipative irreversible processes* across shock waves and *friction phenomena*, which are responsible for heating production;
- *natural convection* and *radiation phenomena* through the external walls of the tube, *thermal longitudinal conductivity* through cavity internal walls, *mass exchange* and *forced convection* between nozzle jet flow and heated gas on the cavity, responsible for heating removal from the cavity.

As regards the latter, the first three heating removal mechanisms could be neglected, while the last two are the most relevant, as it will be described later.

1.4.1 Heating production mechanisms

Shock waves dissipative processes

The main source of heating is certainly the one related to the irreversible processes which takes place across the shock wave front. Brocher and Maresca

[12] referred to temperature-entropy graphic to better define the mechanical energy lost by the shock wave while travelling inside the resonator cavity, which represents the amount of energy related to these non-isentropic processes.

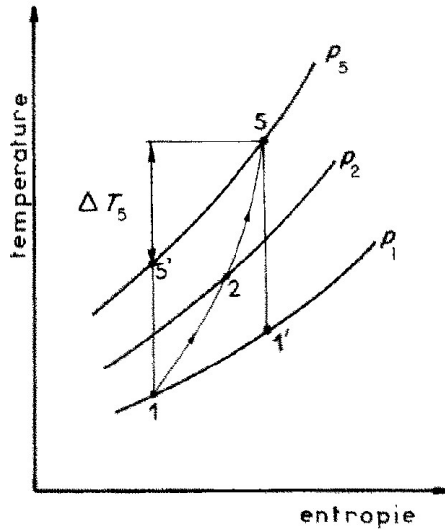


Figure 1.8: Gas flow evolution represented on temperature-entropy diagram [12]

Based on the graphic shown above on *Figure 1.8*, the amount of heat connected to the latter can be calculated as follows:

$$Q_{\text{irr},s} = mC_p\Delta T_5$$

where m is the gas mass, C_p the specific heat at constant pressure and ΔT_5 represents the difference of temperature between diagram points 5 and 5'. The incident shock wave on the graphic is represented with the curve going from point 1 to point 2, while the reflected wave brings the gas flow until point 5. Then, the irreversible processes occurring across shock waves allow the gas flow to transmit its lost energy as heat to the internal cavity walls, so that the first reaches the point 5' on the $T - s$ diagram. After that, the isentropic expansion brings the situation back to point 1. The gas would have been brought instead to point 1' if there had not been any energy dissipation. The mechanical power lost by jet flow related to the aforementioned phenomena can be written as a function of specific heat

ratio γ and Mach number M_2 (defined in *Figure 1.9*) ($\phi_{\text{irr},s}(\gamma, M_2)$) [12].

Friction phenomena

As regards the heating amount due to friction phenomena occurring inside the resonator, a first estimation of the power related to them can be done. It can be said, looking at the distance-time diagram of *Figure 1.9*, that the energy lost for friction by the nozzle jet flow entering the cavity, considering a wall element with a length dx , is equal to [12]:

$$dQ_{\text{fr},\text{in}} = \frac{C_f}{2} \rho_2 u_2^3 \frac{S}{D} (t_2 - t_1) dx$$

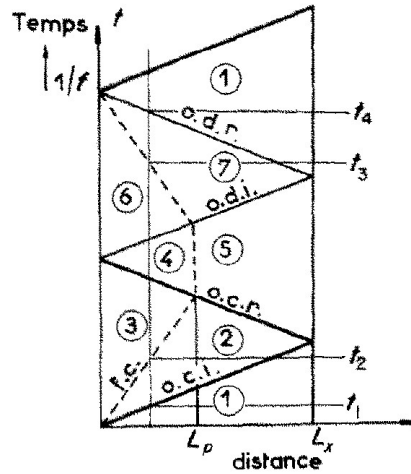


Figure 1.9: *Time-distance diagram of cavity flow relative to a single cycle, with the various flow zones indicated* [12]

where C_f is the friction coefficient, S/D is the ratio between the internal section surface of the cavity and its internal diameter. The flow zone number 2 corresponds to that included between the contact surface and the incident shock wave during the inflow phase. Moreover, if the amount of energy lost by friction phenomena during the outflow phase $dQ_{\text{fr},\text{out}}$ is supposed to be equal to that on the inflow phase, the total energy lost dQ_{fr} will be equal to [12] :

$$dQ_{\text{fr}} = C_f \rho_2 u_2^3 \frac{S}{D} (t_2 - t_1) dx$$

After integrating the previous relation on the cavity length and doing some substitutions, the power related to these friction losses P_{fr} can be obtained as a ratio with the maximum power transferable from the jet flow to the gas trapped inside the cavity by compression P_2 [12]. Their relation will be a function of specific heat ratio, Mach number, cavity length to diameter ratio, and Reynolds number [12], as follows:

$$\frac{P_{\text{fr}}}{P_2} = \phi_{\text{fr}}(\gamma, M_2, L/D, Re)$$

1.4.2 Heating removal mechanisms

Natural convection and radiation phenomena

As regards these two phenomena, it has been demonstrated by Brocher and Maresca that the heat transmitted by radiation and convection from the external walls of the tube to the environment represents only a small part of the energy lost from the nozzle jet flow entering the cavity [10]. It has been also verified, after other experiments, that the endwall temperature is not so affected by the heat convection losses in the jet regurgitant operational mode [29].

Mass exchange

The strong mixing and the large periodic turbulent motion, occurring when the contact surface collides with the reflected shock wave, induces a relevant mass exchange between the cold gas from the nozzle jet and the hot oscillating gas inside the resonance tube, as demonstrated through shadowgraphs in the regurgitant mode by JPL in 1976 experiments [29]. This represents the main heat removal mechanism inside the cavity, with the nozzle cold jet flow removing heat from the heated gas trapped inside the cavity. In particular, during inflow and outflow phases respectively a mass of hot and cold gas passes through the contact surface [12]. Moreover, it can be seen from the graphic on *Figure 1.10* that increasing the Mach number M_2 of the flow zone 2 (*Figure 1.9*) brings to an increase of penetration length L_p . This means that the higher is the Mach number, the more influence the mass exchange heat removal mechanism will have [12], as well as the forced convection which will be described in the next paragraph. As concerns the heat amount lost during the process described above ($Q_{\text{m.ex.}}$), the following relation could be

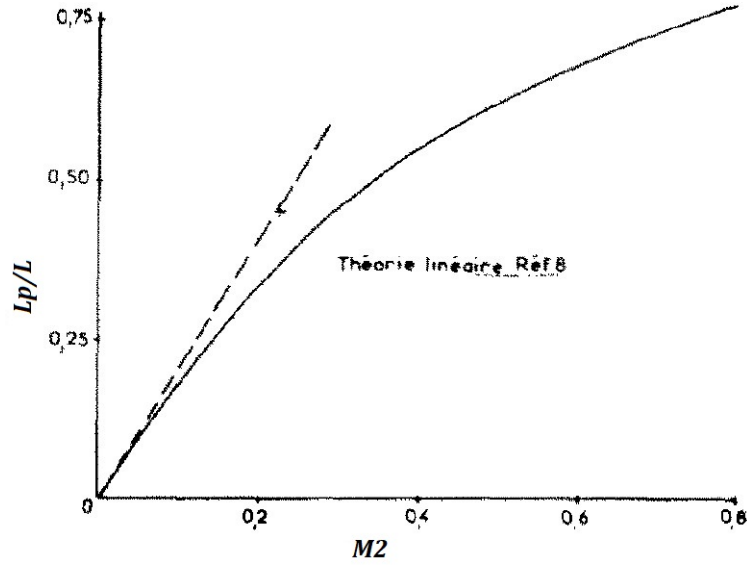


Figure 1.10: Influence of Mach number on penetration length L_p of the nozzle jet flow [12]

written. Therefore, defining m^* as the mass of gas passing through the contact surface (hot gas on the inflow phase, nozzle jet cold gas on the outflow phase), $T_{\text{tot},2}$ and $T_{\text{tot,jet}}$ respectively as the stagnation temperature of the hot gas trapped into the cavity and that of the nozzle jet, the relation will be [12]:

$$Q_{\text{m.ex.}} = m^* C_p (T_{\text{tot},2} - T_{\text{tot,jet}})$$

As done above while describing the friction phenomena (*Section 1.4.1*), the power related to mass exchange processes ($P_{\text{m.ex.}}$) in relation to maximum power which can be transferable by compression from nozzle jet flow to cavity hot gas (P_2) [12]:

$$\frac{P_{\text{m.ex.}}}{P_2} = \phi_{\text{m.ex.}}(\gamma, M_2, L/D, Re, m^*) \left(\frac{\theta - 1}{\theta} \right)$$

with $\theta = T_{\text{tot},2}/T_{\text{tot,jet}}$.

The previous ratio is a function of specific heat ratio, Mach number, cavity length to diameter ratio, Reynolds number and previously defined mass m^* , similarly to friction phenomena related power seen before. Otherwise, in this case it can be seen an additional dependence from the ratio between the two

temperatures of cavity gas and nozzle jet flow θ .

Forced convection

The heat transmission between the internal walls of the resonator tube with, alternatively, hot gas inside the cavity and nozzle jet cold gas represents another source of heat removal because of forced convection phenomena. In order to know the amount of heat removed through forced convection a study of the boundary layer development should be performed, as done by Brocher and Maresca [12]. The main hypothesis made for this study consists in considering the boundary layer of the cavity hot gas as it was completely developed, neglecting the oscillating nature of the latter [11]. It is possible to estimate the amount of energy transferred in the form of heat from the gas heated in the resonator to its internal walls as follows [12]:

$$Q_{fc} = 2\pi D h_2 \int_0^{L_p} [T_r - T_p(x)](t_2 - t_1) dx$$

where T_r is the hot gas recovery temperature, $T_p(x)$ the wall temperature at some point x along the tube, $\pi D dx$ the surface of infinitesimal length dx affected by convective heat transfer, h_2 the convective transfer coefficient on the flow area between contact surface and incident shock wave, as depicted on time-distance graphic (*Figure 1.9*), with time difference $(t_2 - t_1)$ referred to the latter. The power related to the heat removed through forced convection can be written in the same way as it has been done for mass exchange in the previous paragraph, having also the same form and parameters dependency when related to nozzle jet flow maximum power P_2 .

1.4.3 Power thermal balance

After having seen and analyzed the various phenomena related to heating production and removal inside the cavity, a thermal balance must be done as a final step to evaluate the thermal equilibrium of the cavity. The heat production due to shock wave dissipative processes and friction phenomena are limited by heating removal processes mainly due to hot and cold gas mass exchange inside the cavity and forced convection. Hence, the following

relation can be written [12]

$$P_{\text{irr,s}} + P_{\text{fr}} = P_{\text{m.ex.}} + P_{\text{fc}}$$

with the power level written above having been defined in the previous paragraphs. It can be also possible to better visualize the weight of every single power contribution to the total thermal balance and how they change in relation to Mach number, as done by Brocher and Maresca [12]. The graphic below (*Figure 1.11*) shows the trend of the functions ϕ_i which define the different power levels involved in the themal balance equation. It can be seen that the functions related to shock wave irreversible processes and friction phenomena ($\phi_{\text{irr}}, \phi_{\text{fr}}$ on the graphic) increase with Mach number, whereas those related to the heating removal mechanisms (mass exchange, ϕ_{m} and forced convection, ϕ_{cf}) decrease with M_2 .

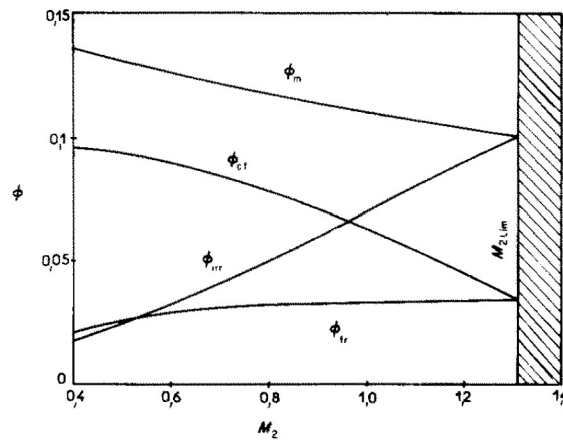


Figure 1.11: Variation of ϕ functions related to Mach number M_2 , for air at ratio $L/D = 33$ [12]

1.5 Resonance igniter operating modes

Studies conducted by Sarohia and Back [28] about 40 years ago demonstrated that three different operating modes characterize the functioning and the thermal effects obtained in the resonance igniter. They are the following:

- ***Jet Instability Mode (JIM)***, occurs at subsonic, undercritical Nozzle Pressure Ratio ($NPR < 1.9$ [32]) (with NPR equal to the ratio between nozzle total pressure and ambient static pressure, as defined later in *Section 1.6*). It is induced by vortex shedding originating from the nozzle outlet which travels downstream, causing weak pressure waves inside the resonator [17]. Practically, it is not of further interest since it does not produce large heating effects. When NPR exceeds the critical limit the heating effects of the phenomena start to be relevant, and two more operating modes could be identified;
- ***Jet Regurgitant Mode (JRM)*** is characterized by an *inflow phase* when the jet free-stream enters inside the cavity travelling towards its endwall, and an *outflow phase* when the gas leaves the resonator, emptying it and starting a new cycle. In most of the cases this operational mode occurs when the resonator inlet is placed near the free-jet Mach disk, and the oscillations generated possess approximately the frequency of the first acoustic longitudinal mode of the cavity [7]. *JRM* becomes the predominant mode for supersonic jets if the nozzle-cavity distance is higher than that corresponding to the first shock position of free jet [32]. In the beginning of the oscillation process a series of weak shock waves detached from the bow shock enters the cavity, eventually coalescing to single stronger shocks if the latter is long enough. This can cause a complete emptying and re-filling of the cavity at every cycle, but under certain condition a portion of the gas near the end of the tube can remain inside it being repeatedly compressed and heated, as described in *Section 1.2*. Consequently, the gas temperature can overcome the stagnation temperature at the closed end of the resonator. As regards the static pressure in the cavity, it can oscillate between two values, which are beyond the total pressure of the nozzle and below the ambient pressure, due to the strong oscillations.

- **Jet Screech Mode (JSM)**, observed for $NPR > 3.9$ [32] and characterized by weak pressure oscillations induced by the vibration of a normal shock placed in front of the cavity, at frequencies much higher than in the previous case of *JRM* (about 20KHz) [32]. Because of this, the mass exchange between the cavity and the surrounding fluid is strongly reduced. The location, strength and oscillation frequency of normal shock is determined by nozzle-cavity gap and NPR [32]. It has been observed that strong thermal effects occur in *JRM* when the resonator has a high length-to-diameter ratio, while for short resonators *JSM* is the operating mode which allows to obtain higher temperatures [7].

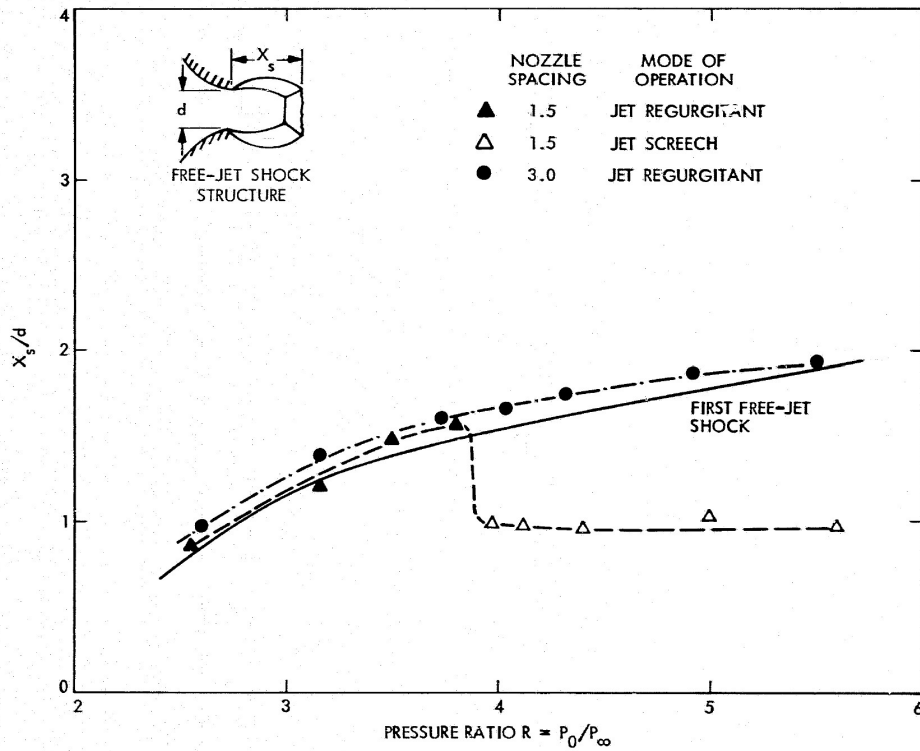


Figure 1.12: First shock location related to nozzle pressure ratio, for different nozzle-cavity distances [29]

As regards the transition between jet regurgitant and jet screech modes, it has been experimentally seen that as the pressure rises, the position of free-jet shock (X_s/d) increases, until it becomes equal to the distance between nozzle exit and cavity inlet [29]. For higher values, the resonator switches to screech mode, depending however on the amount of nozzle-cavity distance, as depicted on *Figure 1.12*.

1.6 Driven parameters of resonance heating

As previously mentioned in *Chapter 1.1*, resonance heating phenomenon is influenced by some parameters which can be:

- jet flow pressure parameters (*nozzle pressure, nozzle pressure ratio (NPR)*);
- resonator geometrical characteristics (*nozzle diameter, nozzle-cavity distance, cavity length, diameter, shape*);
- *resonator material*;
- *gas composition*.

1.6.1 Nozzle Pressure / NPR

Nozzle exit pressure is one of the parameters which determines the achievement of the maximum attainable temperature having determined geometrical properties of the apparatus. Its influence can be seen in relation to the pressure oscillations amplitude as depicted on the graphic of *Figure 1.13*, which shows a linear increasing of pressure waves amplitude with increasing nozzle pressure and decreasing NPR [27]. *NPR (Nozzle Pressure Ratio)* defines the ratio between the total pressure at the nozzle exit, equivalent to the feed pressure upstream the nozzle considering an isentropic expansion (p_n), and the downstream static pressure (p_e).

$$NPR = \frac{p_n}{p_e}$$

The variation of the endwall temperature as a function of NPR is depicted on the graphic on *Figure 1.14*. In this case, it can be observed a parabolic trend with a maximum temperature at a certain NPR value depending on the apparatus parameters.

1.6.2 Nozzle-cavity distance

Another important factor which influences resonance heating is the distance from nozzle exit to cavity inlet (s), which can be expressed in relation to the nozzle diameter (d) as a s/d ratio. First, the latter influences the jet stream

1.6. Driven parameters of resonance heating

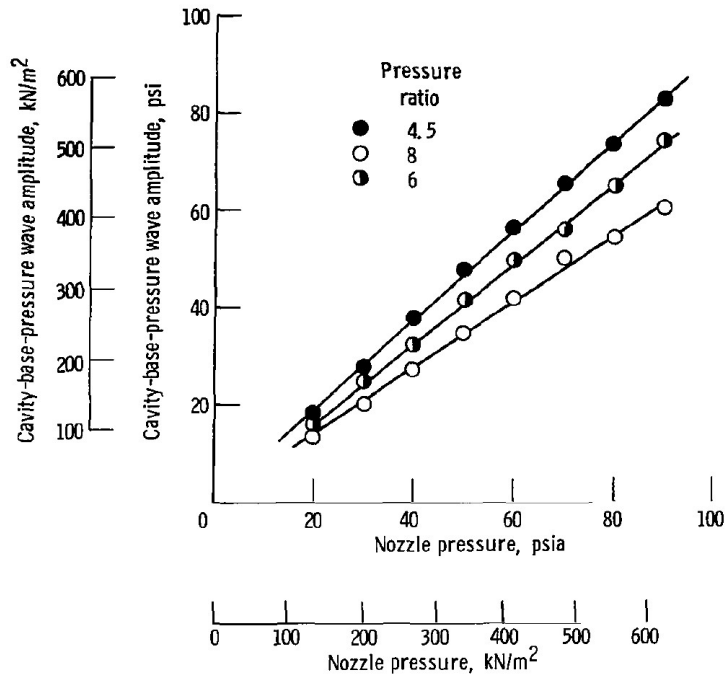


Figure 1.13: Influence of nozzle pressure on pressure waves amplitude, for different NPR values (brass conical cavity, nitrogen, nozzle-cavity gap: 0,45 inch) [27]

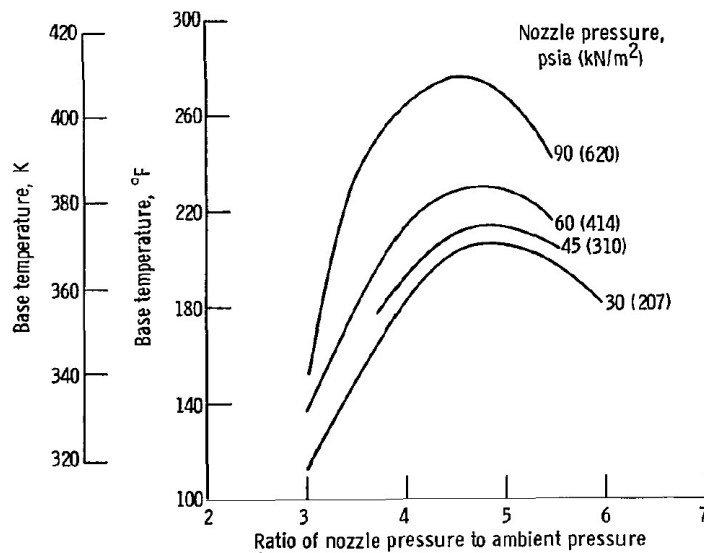


Figure 1.14: Influence of NPR on endwall temperature, for different nozzle pressure values (brass conical cavity, nitrogen) [27]

pressure which shows some peaks in the compression regions (between dash lines) which, in turn, represent the instability region mentioned in *Section 1.2*, as seen on the graphic of *Figure 1.15*. After experiments conducted with

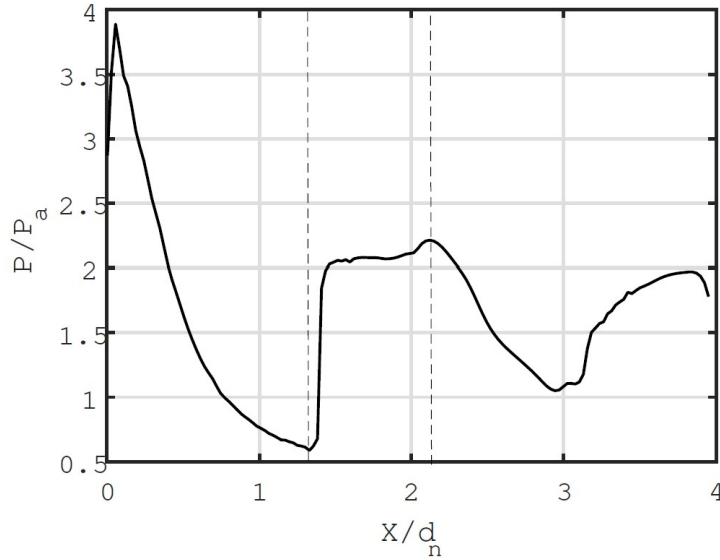


Figure 1.15: *Dimensionless pressure at the jet centerline as a function of dimensionless nozzle-resonator distance* [15]

different NPR, it has been seen that nozzle-cavity gap is indirectly affected by it because of different positions assumed by the cell boundary, in relation to NPR. Hence, the bow shock will vary its position within the unstable zones of the jet flow field. A free jet has been considered during these experiments because its structure remains fairly constant regardless of the presence of the cavity in front of nozzle exit [27], and also for simplicity. As a consequence of this succession of relations, a value of nozzle-cavity gap which maximize the endwall temperature will exist, assuming a fixed NPR and nozzle diameter (and so, nozzle pressure). This situation is showed on *Figure 1.16* where the positions of first cell boundary and cavity inlet are compared. The distance between the two curves represents the bow shock standoff distance [27]. As a complement to the previous results, the variation of the endwall temperature in relation to the nozzle-cavity distance is depicted on *Figure 1.17*. There is, therefore, a certain value of the latter that give the best resonant coupling [27] and is determined by fixing only NPR and nozzle diameter.

1.6. Driven parameters of resonance heating

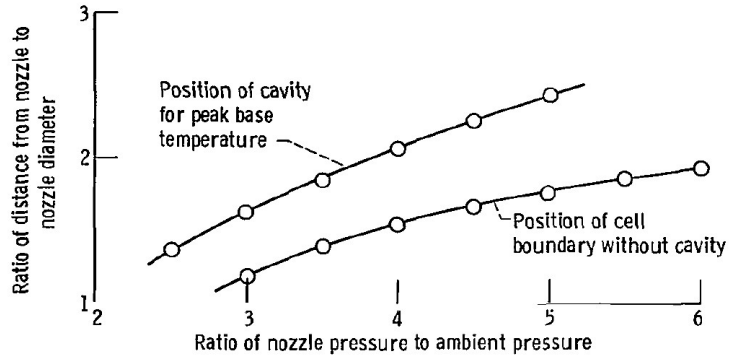


Figure 1.16: Position of first cell boundary and inlet cavity position related to peak endwall temperature, for different NPR values [27]

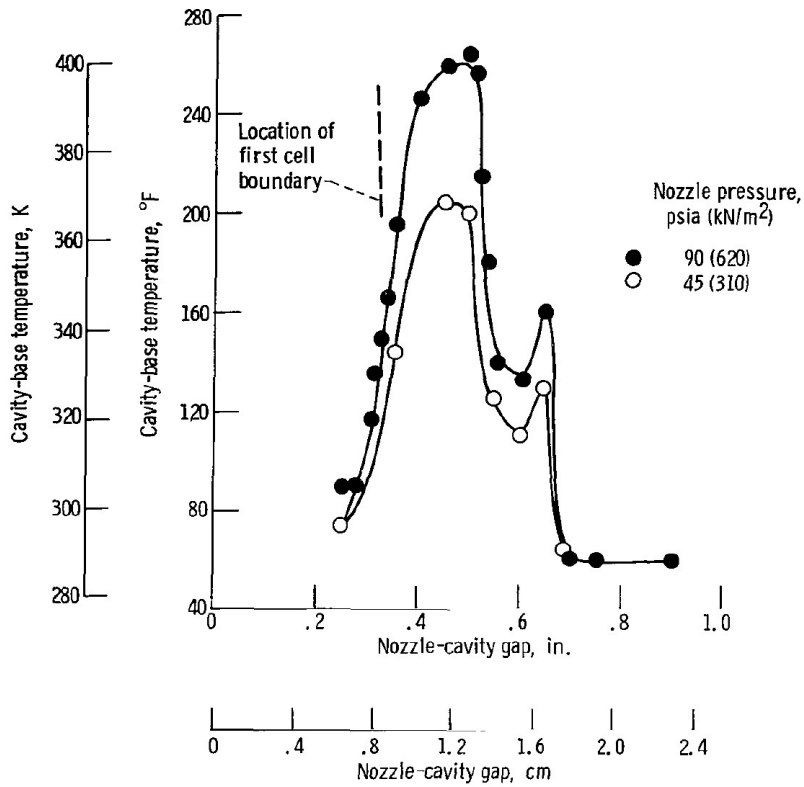


Figure 1.17: Cavity endwall temperature variation related to nozzle-cavity distance, for different values of nozzle pressure [27]

1.6.3 Cavity depth

A variation on cavity depth leads to a variation of the distance travelled by compression waves oscillating within the resonance tube. This increases their tendency to coalesce into shock waves thus producing an increase in pressure wave amplitude [27], as it can be observed on top of *Figure 1.18*. It can be seen that while increasing cavity depth a maximum pressure wave amplitude will be reached, remaining relatively constant at a pressure level close to that of the nozzle for higher values of depth (in this case, $p_n = 3.1$ bar) [27]. In addition, an increase in the wave period can be observed due

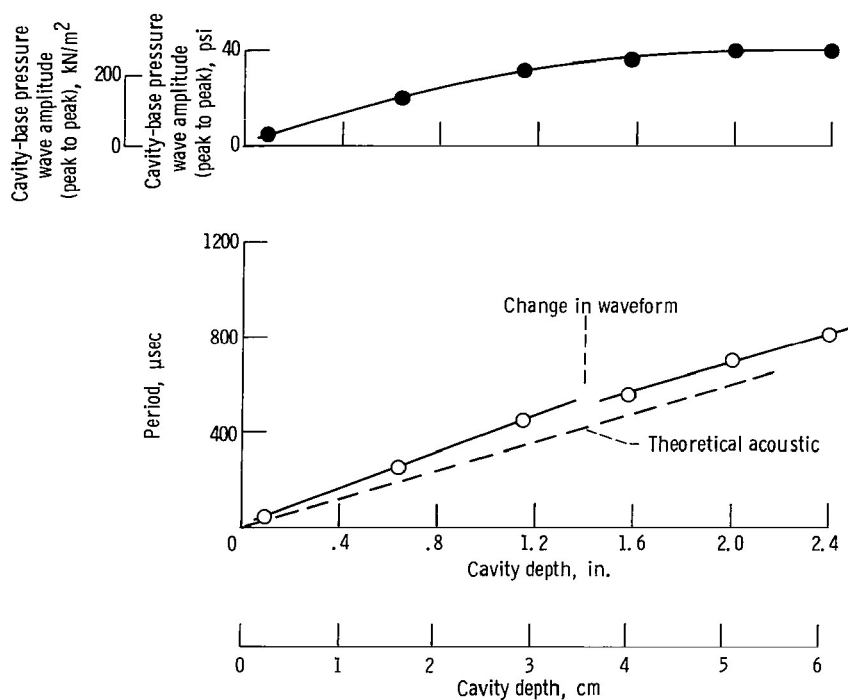


Figure 1.18: *Cavity endwall pressure waves amplitude (top) and period variation (bottom) related to different values of cavity depth [27]*

to an increase of pressure waves travel length inside the resonator (*Figure 1.18, bottom*). As depicted, at some value of cavity depth a transition from a sinusoidal waveform to a shock-type one occurs because of the combination of compression waves, as said before.

The increase in resonator tube depth produces, instead, an opposite effect on the temperature. In fact, as it can be observed below from *Figure 1.19*, the

latter will mainly decrease because of the increase of the surface for thermal conduction and convection losses [27].

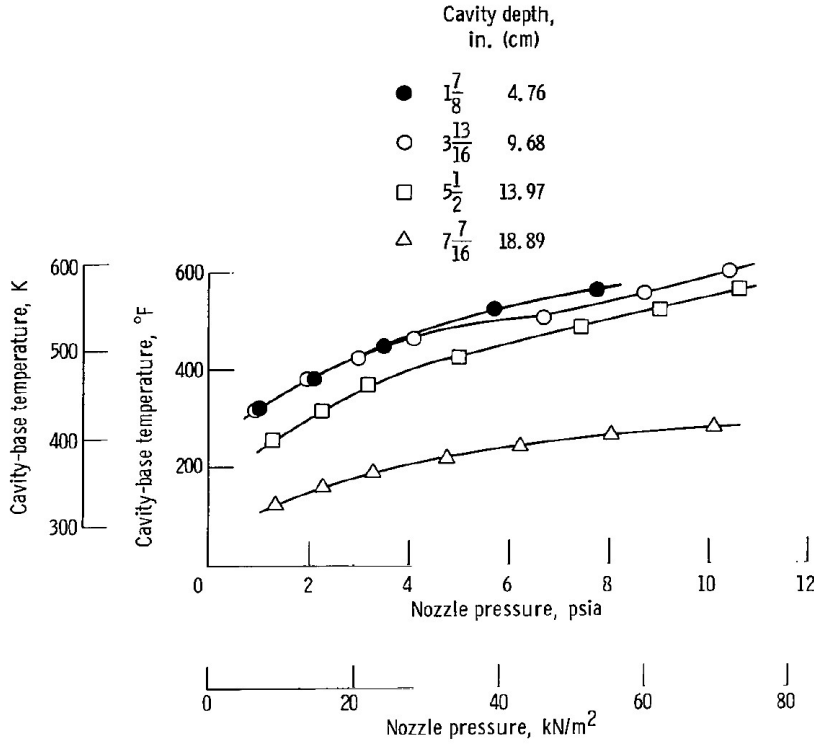


Figure 1.19: Variation of cavity endwall temperature related to nozzle pressure, for different values of resonator depth [27]

1.6.4 Cavity shape

Another geometrical factor to be considered in order to analyze resonance heating phenomenon is the shape of the resonator tube. Typically, cylindrical and tapered resonator shapes have been considered for testing, with the latter having been proved superior in terms of heat input per unit of time [26]. The difference between the two shapes can be assessed looking at the graphic of *Figure 1.20* [27], where the temperature reached at the tapered cavity endwall is more than doubled in respect to normal cylindrical resonator even at low nozzle pressure values, with a resultant steeper heating rate. In the graphic of *Figure 1.21* a tapered cavity with a cylindrical extension is also considered, compared with the normal tapered one [27]. As it can be observed, a decrease

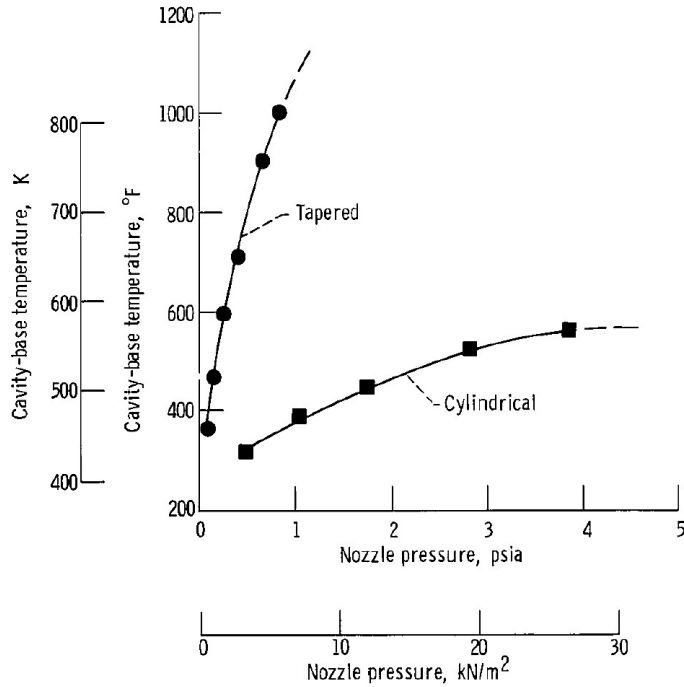


Figure 1.20: Influence of resonator shape on endwall temperature, for different nozzle pressure values [27]

in efficiency for the extended tapered resonator is assessed, because of the presence of the extension which increase the cavity length hence decreasing the endwall temperature for a given nozzle pressure, as seen on the previous paragraph (*Section 1.6.3*).

On the last case (*Figure 1.22*) a further comparison is made between tapered and 3-steps resonator configurations [8], with the latter presenting a step variation in diameter along its length, as shown on *Chapter 2*. As seen from the graphic, besides confirming the higher effectiveness of normal tapered resonator, using air as jet flow gas instead of methane allows to reach higher temperatures.

1.6.5 Resonator materials

After having considered geometrical properties of the resonator tube and the influence of pressure, the materials of which the resonator could be composed can now be analyzed because of their important role in achieving the max-

1.6. Driven parameters of resonance heating

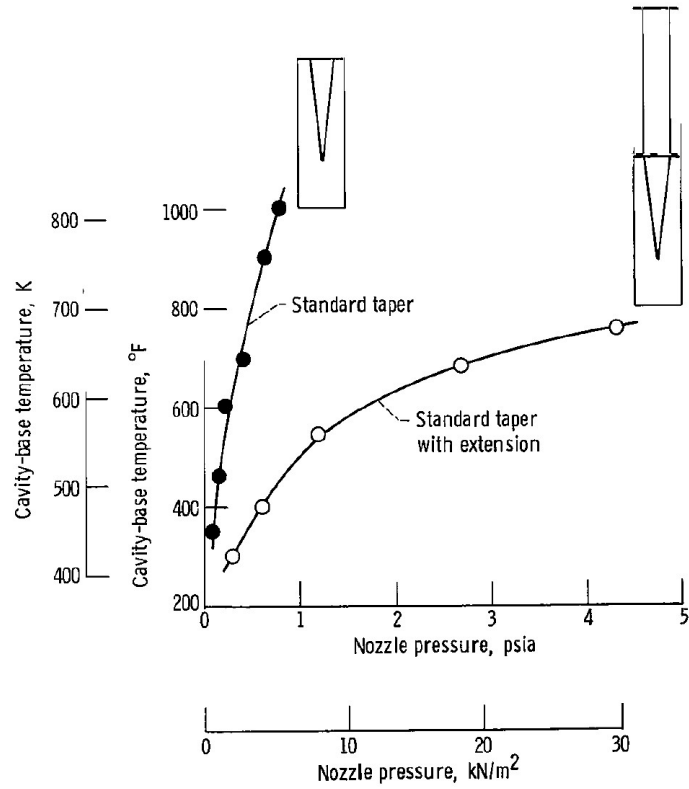


Figure 1.21: Differences in endwall temperature between standard and extended tapered resonator configurations [27]

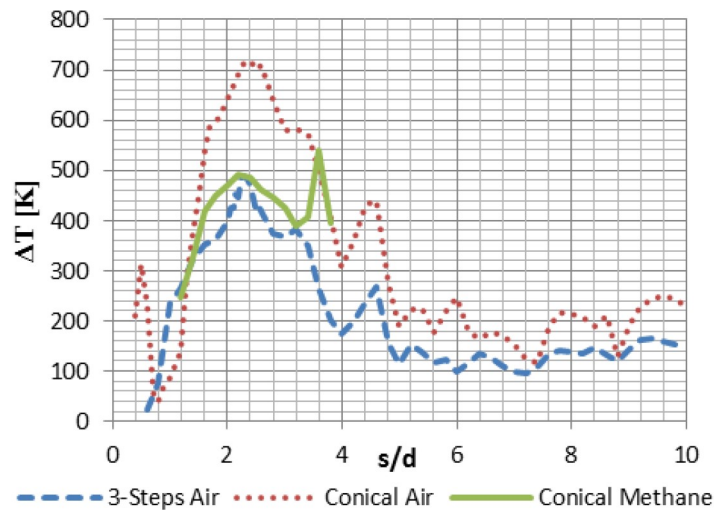


Figure 1.22: Temperatures reached with tapered (conical) and 3-steps resonators ($NPR=4$) [8]

imum temperature needed for propellant ignition, as well. In fact, thermal properties of those materials must be considered in order to have a low thermal conductivity, a high mechanical strength, but also a material which can operate at high temperatures. On their experiments, Brocher and Ardissone [9] tested *wood*, *durestos* (made of asbestos fibers and phenolic resin) and *MACOR* (machinable ceramic made by Corning Inc.) as materials for the resonator. As it can be observed below from *Figure 1.23*, wood has been found being the best solution thanks to its very low conductivity (about $0,05W/m * K$), with durestos having a low thermal conductivity but low resistance to high temperatures and MACOR being the highest conductive material but really useful for high temperatures. These experiments were conducted using helium as gas and with a normal cylindrical cavity.

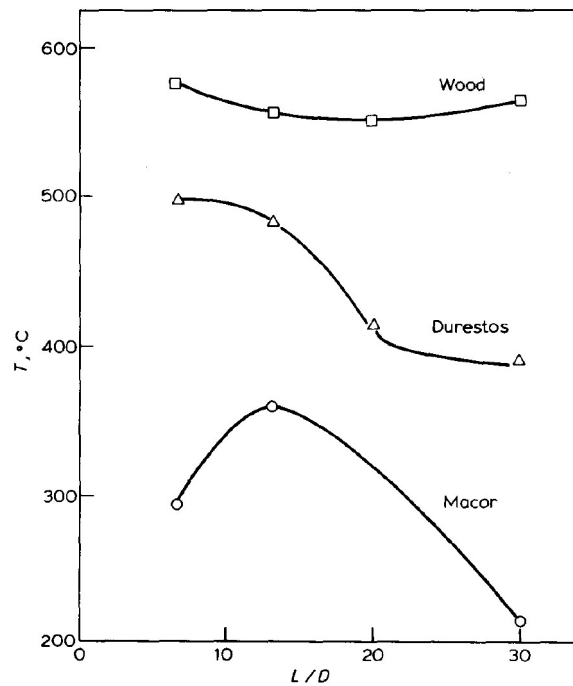


Figure 1.23: *Temperatures on resonator cavity endwall related to nozzle-cavity distance / nozzle diameter ratio (L/D), for different materials [9]*

Other materials taken into account for further experiments have been the *zirconia* which possesses a very low thermal conductivity, a high strength but unfortunately a high porous structure which absorbs pressure waves. This materials, together with *asbestos composites*, *pyrolytic graphite* and *brass*

among the others, have been used by Phillips and Pavli during their experiments [27]. Tests conducted by Brocher and Ardissonne [12] exhibited considerable differences in temperature on the cavity base of two cylindrical resonator tubes made of platinum and iron with different thickness (0.1mm for the first, 0.5mm for the second). *Figure 1.24* shows this situation highlighting the central role of resonator tube thickness in limiting thermal losses through the tube walls. Moreover, a comparison between iron and wood has also been made, using a square-section tube, which showed even a bigger difference in endwall temperature than on the previous case [12]. As depicted on (*Figure 1.25*), the difference here is more remarkable mostly due to insulating properties of wood. In both graphics, x/L represents the fraction of the total tube length, therefore $x/L = 1$ indicates the cavity base.

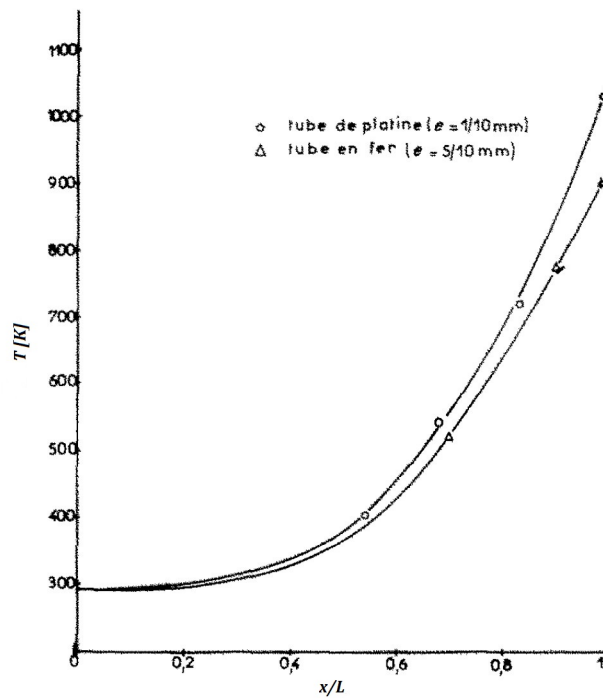


Figure 1.24: Influence of materials and tube walls thickness on temperature along a cylindrical cavity (Helium, jet flow $Mach=0.96$) [12]

Finally, polytetrafluoroethylene (*PTFE*), which is a fire-proof polymer, has been used as well on tests carried out by Afzali and Karimi [4] in 2017 because of its high-temperature resistance and the low thermal conductivity.

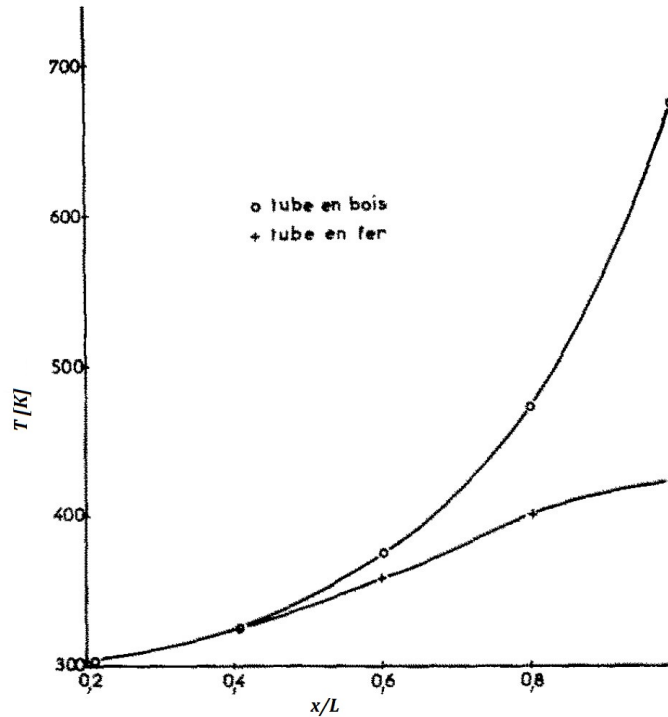


Figure 1.25: Temperature variation along two square-section cavity made of wood and iron (Air, jet flow Mach=0.84) [12]

1.6.6 Gas composition

The gases or gas mixtures used to carry on various tests during the years revealed the importance of their influence over the resonance heating phenomenon, showing considerable differences between one another. The first example can be observed on *Section 1.6.4* from *Figure 1.22* which refers to tests conducted by Bauer, Pauw and Haidn in 2014. In this case, changing from *methane* to *air*, using a cylindrical cavity, permits to increase the endwall temperature of about 200K [8]. Differences between *hydrogen* and *nitrogen* have been demonstrated during the tests conducted by Phillips and Pavli, which used a tapered cavity. As seen from *Figure 1.26*, the clear superiority of hydrogen in increasing the temperature of cavity base, which reaches high temperatures even at low nozzle pressures, is assessed [27]. This can be explained looking at the different molecular weight of the two gases, which influences sonic velocity and allows hydrogen to have an oscillating frequency about three times higher than that of nitrogen. This, in turn, brings

1.6. Driven parameters of resonance heating

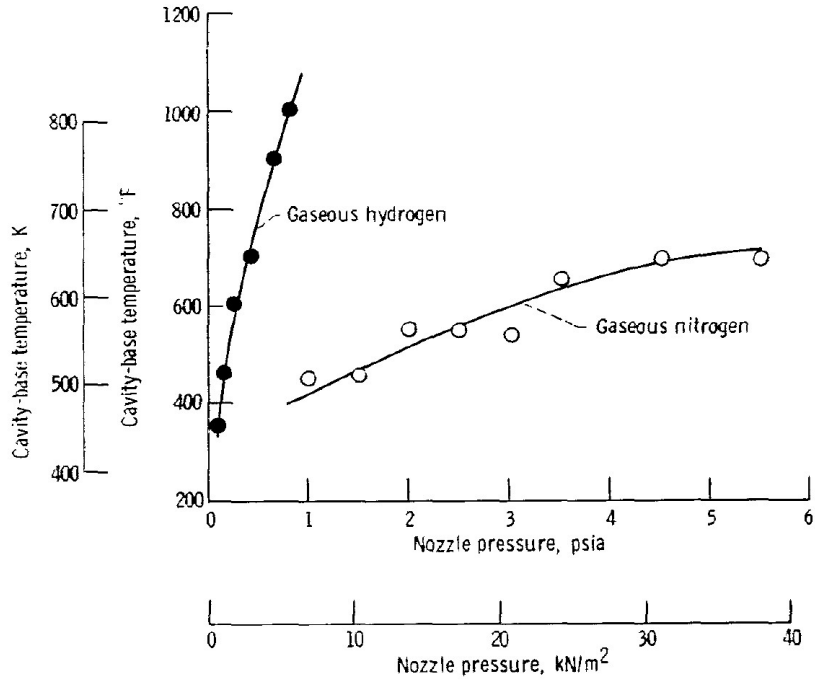


Figure 1.26: Influence of gas composition (H_2 , N_2) on cavity endwall temperature, related to nozzle pressure ($NPR=4.5$, nozzle-cavity gap=0.45 inch) [27]

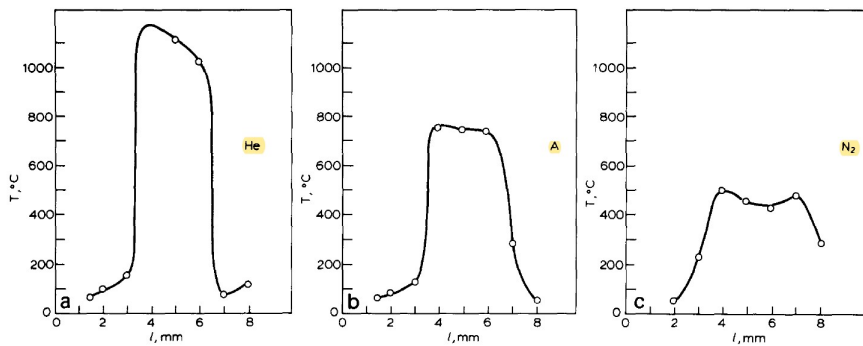


Figure 1.27: Influence of different gases on cavity endwall temperature, for different nozzle-cavity gaps (from left to right: Helium, Argon, Nitrogen; stepped-cavity, $p_n=7$ bar) [9]

to have more energy per unit time (about three times as much) in the case of hydrogen. As regards the nitrogen, if it is substituted with oxygen results are very similar [27]. Other gases have been studied as well, as it can be observed from the graphic of *Figure 1.27* which refers to experiments conducted by Brocher and Ardissonne [9]. The higher performances of hydrogen against those of nitrogen and also *argon* are once again confirmed.

1.6.7 Other parameters

Mach number of nozzle jet flow

As regards the jet flow coming from the nozzle, it can be seen that depending on its Mach number a higher or lower temperature can be obtained at the cavity base. Observing these variations along all the cavity (*Figure 1.28*), it can be seen an increase of temperature while increasing the Mach of the jet flow, with the most relevant differences located near the endwall ($x/L=1$) [12].

Thermal insulation of resonator tube

A mention has to be done about the influence of external thermal insulation in improving the effectiveness of resonance heating process, because of the reduction of convection and radiation thermal losses around the tube. From *Figure 1.29* remarkable effects can be seen only on the last part of the cavity ($x/L>0.8$) with the maximum temperature difference located at the cavity endwall, as expected [12]. On the results represented on the graphic, a thick sleeve made of glass wool has been used as an external thermal insulation [12].

Roughness of cavity walls

The level of roughness has a negligible influence on elevating the temperature inside the cavity. Based on the studies conducted by Brocher, Maresca and Albertini [5] a slightly higher temperature can be observed only on small dimensions tubes.

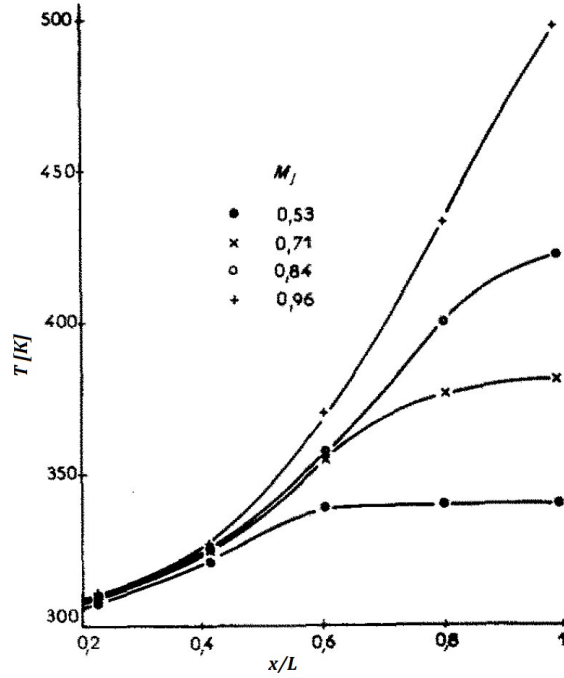


Figure 1.28: Influence of nozzle jet flow Mach number on temperature along the cavity [12]

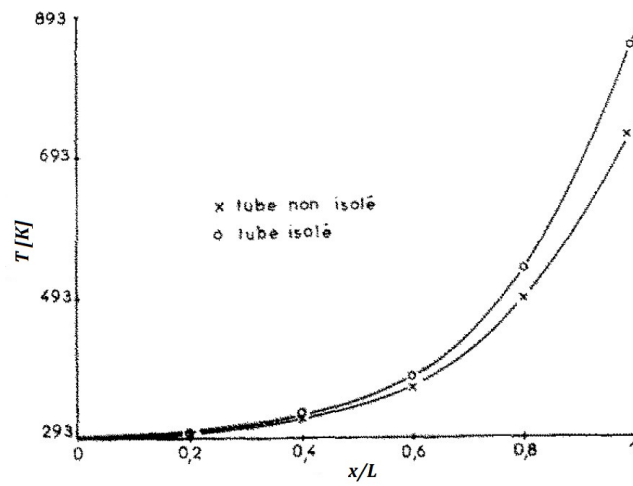


Figure 1.29: Differences on achieved temperature along the cavity, for resonator with and without thermal insulation [12]

Chapter 2

Experimental apparatus

2.1 Preliminary setup considerations

Different experimental studies have been carried out to develop an igniter based on resonance heating principles. The present work partly follows the experimental studies conducted by TUM [8], as regards only the geometry of the resonator cavity configurations, while different materials have been used. Moreover, their experimental configuration included a vacuum chamber enclosing the resonator to prevent convective heat losses and optically accessible to better understand the effects of resonance ignition phenomenon [8].

However, in this study the main objective was that of validating the resonance heating phenomenon by designing an experimental apparatus and successively performing a test campaign. For the experimental tests two different types of resonator cavities have been used:

- a *3-steps configuration* cavity which shows three different diameters along its length, as depicted in *Figure 2.1 (above)* ;
- a *conical* cavity tapered along the jet flow axis, showing two different diameters at both inlet and endwall (*Figure 2.1, below*).

The first configuration has been used during the initial tests as a prototype to validate the resonance heating process inside the cavity. After having validated the actual presence of the phenomenon, the conical configuration has been mounted on the experimental apparatus during the following phase

of improvement of the entire facility.

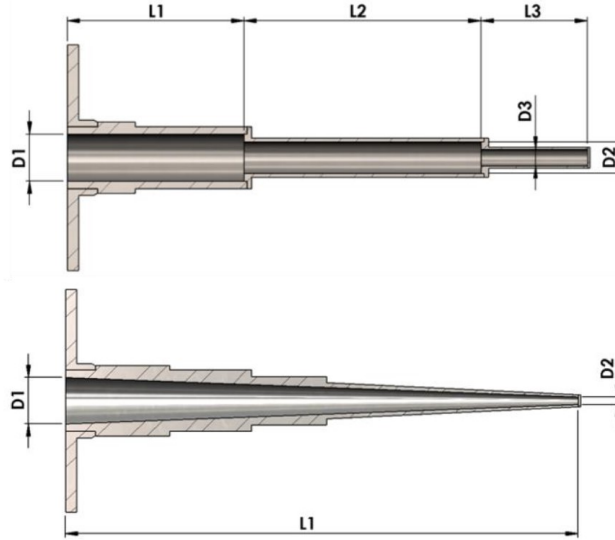


Figure 2.1: Cavity configurations: 3-steps (above), conical (below) [8]

2.2 Description of components

2.2.1 Resonator configurations

The resonance cavity, and in general the resonator, is the most important component of the entire facility allowing to perform tests for the study of resonance heating process. As previously said in *Section 2.1*, the *3-steps configuration* has been used during the first phase of phenomenon validation test campaign, whose dimensions could be seen from the drawing of *Figure 2.2*.

Two different materials have been used within this configuration:

- *wood*, with the cavity directly cut inside it ;
- *poly-methyl-metacrylate (PMMA)*, which is also used as fuel propellant in hybrid rockets.

The PMMA version of 3-steps resonator could be seen on *Figure 2.3*. Apart from the materials, the other dissimilarity between the two versions of this component is the different placement of thermocouple, as it will be seen after on *Section 2.4.1*. Moreover, the wooden 3-step cavity has been only used

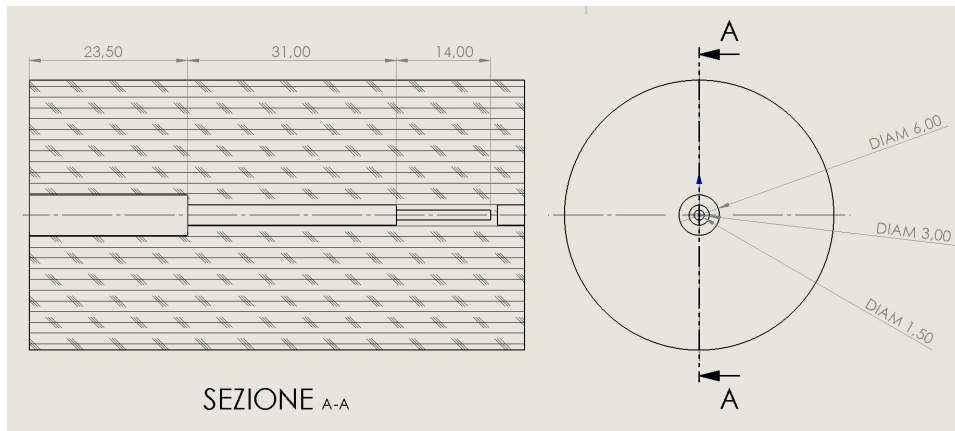


Figure 2.2: 2-D drawing of both 3-step resonators (wood, PMMA) used for validation tests

in the context of a first validation attempt to record at least a minimum temperature increase, looking more for a refining of the total facility configuration rather than obtaining significant test results.



Figure 2.3: PMMA resonator used for validation tests

The other configuration used for the resonator is the conical (or tapered) one, whose 3-D design and related dimensions are showed respectively in *Figure 2.4* and *Figure 2.5*. It has been made using the DMLS (Direct Metal Laser Sintering) additive manufacturing technique, which uses a laser beam

to sinter a powdered material, following a previously designed 3-D model of the object to be manufactured.

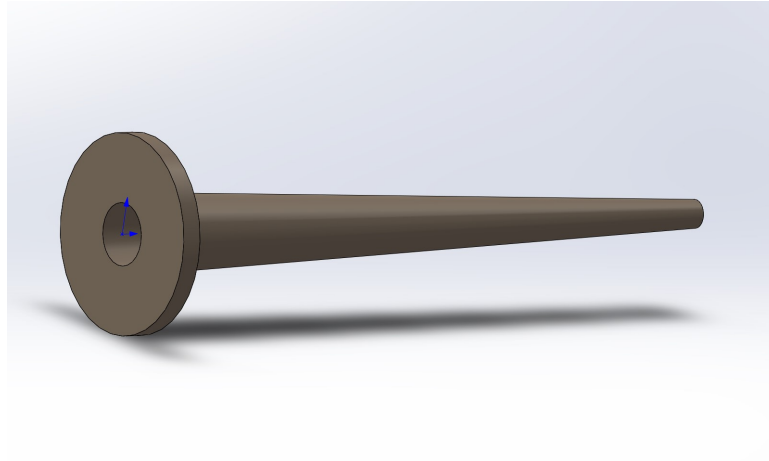


Figure 2.4: 3-D model of conical resonator (final configuration) used for final tests

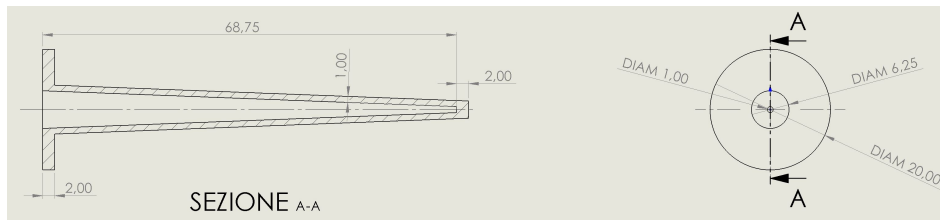


Figure 2.5: 2-D drawing of conical resonator (final configuration) with dimensions

As it can be seen on 3-D model, a flange has been designed to make easier for the resonator to be attached to any fixed support component and consequently withstanding the pressure loads to which it is subjected. The material used to make it has been Inconel[®] 625 (a Nickel-Chromium-based superalloy) in the form of powder. In order to assess the structural strength of the component, a stress analysis has been performed as well. In particular, the Factor of Safety (FOS) distribution along the resonator has been determined as shown on *Figure 2.6*. The parts highlighted in red (resonator tube, flange front base near tube joint) are the most solicited, with a pressure load of 8 bar applied from the inside out and a FOS equal to about 8 which is largely above the typical minimum values assumed for this parameter. It has been chosen to fix the conical resonator by inserting it into a wooden

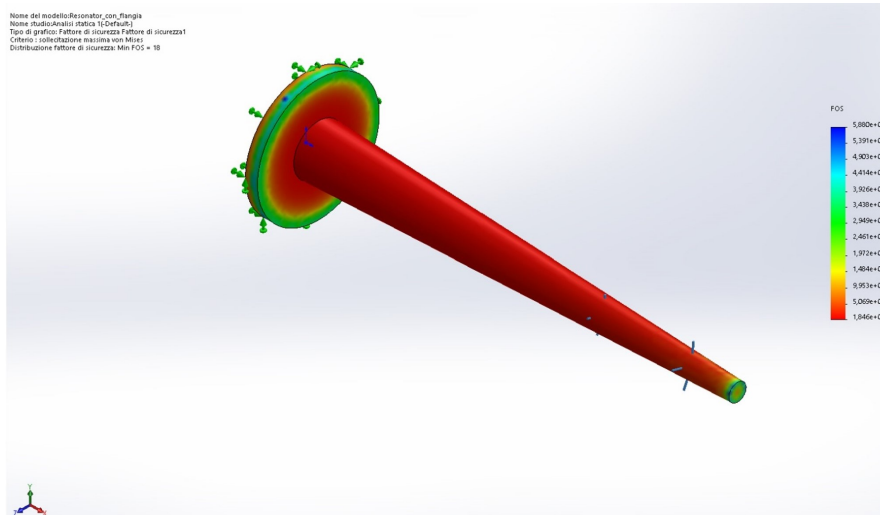


Figure 2.6: Safety factor (*FOS*) derived from stress analysis on conical resonator

block, then attaching the latter to a holed table by means of screws as shown later on *Section 2.4.2*.

2.2.2 Thermocouple

In order to measure the temperature at the cavity endwall a thermocouple has been used for all the tests. Thermocouples are electrical devices formed by two wires made of different metallic materials (called thermoelements) joined at two ends, called hot and cold junctions. When the temperature of one junction is different from that of the other one, a voltage difference is measured between the wires on the cold junction side because of the diverse materials which wires are made of. This thermoelectric phenomenon is referred to as Seebeck effect and consists in the production of an electromotive force whenever a temperature gradient exists between the two materials. Consequently, an electric potential can be measured between the two wires made of dissimilar materials on the cold junction. This potential could be written as follows [30]:

$$\int_{T_1}^{T_2} (S_1 - S_2) dT = (S_2 - S_1)(T_2 - T_1)$$

, where S_1 and S_2 are respectively the Seebeck coefficients related to the two materials of *wire 1* and *wire 2*. Generally, the coefficients depends on the material and on the temperature, but in this case they are considered linear inside the operative range of the thermocouple.

Figure 2.7 below represents a basic thermocouple circuit. The hot joint is immersed into the environment where the temperature level must be measured (in this case, on the external side of the resonator endwall), while the cold joint is connected to a voltmeter to measure the voltage produced between the wires (in this case, to one of the Compact Fieldpoint connector blocks, which will be described later on *Section 2.3.1*).

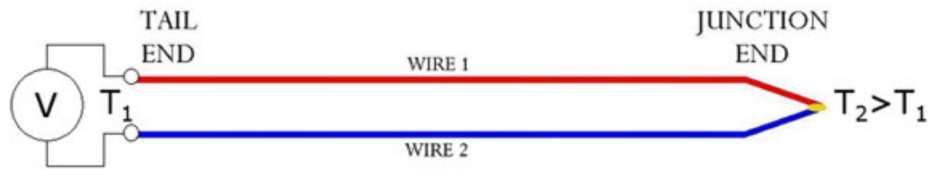


Figure 2.7: Basic scheme of a thermocouple [30]

Thermocouples are very reliable temperature sensors, with a high sensitivity to sudden changes in temperature, but they have some limitations. The main of them consists into its not so high accuracy and the non-linear nature of such sensors. Different types of thermocouples made with various materials exist, having different temperature ranges and usages. The graphic on *Figure 2.8* shows the operating temperature ranges of theirs, while considering the electromotive force produced at different temperatures as well. The sensor used for the tests is a *K-type thermocouple* which is the most common between these thermal sensors, and could measure temperatures up until about $1400K$ as seen from the graphic with a temperature variations sensitivity of $41 \mu V/^\circ C$. However, it is not well suitable to operate in an environment with the presence of many vibrations. It is composed of Chromel (Ni,Cr alloy) and Alumel (Ni,Al,Mn,Si alloy) and operates really well in ambients rich in oxygen. Moreover, the maximum temperatures expected to be measured at the cavity base are comprised within the operating range of this type of thermocouple. There is an additional distinction between thermocouples depending on the sheathing configuration, as depicted on *Figure 2.9*. In fact, the latter determines the response time and whether the hot junction

would be physically and chemically protected. The choice for the experimental tests has fallen on the exposed bead thermocouple, because of its faster response even if this configuration provides no protection from physical and chemical damage.

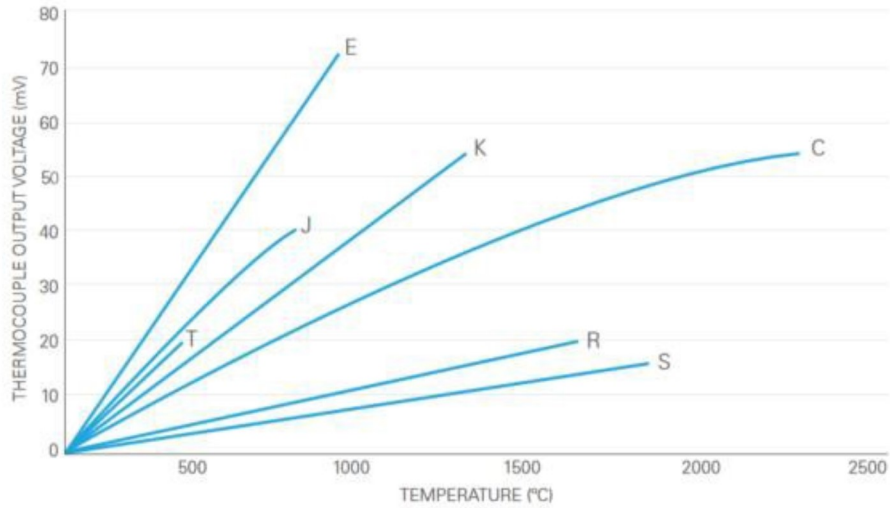


Figure 2.8: *Temperature ranges and output voltages for different types of thermocouples [21]*

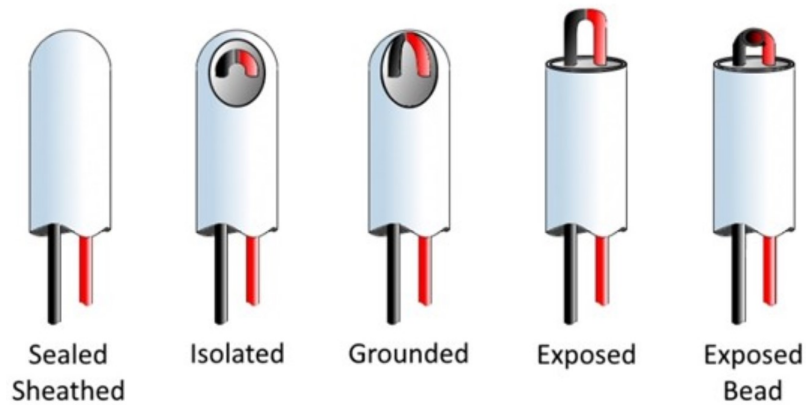


Figure 2.9: *Different configuration of thermocouples sheathing [21]*

2.2.3 Pressure transducer

In addition to thermocouple, another type of sensor utilized during this experimental work has been a pressure transducer. Its main scope was that of increasing the accuracy of pressure level measurement upstream the nozzle jet. Therefore, it has been placed between compressor and nozzle by means of metallic pipe junctions, even if the first possessed its own manometers. The sensor chosen to be mounted on the tests facility belongs to *Wika*[®] *A-10* general purpose-pressure transducers family, and it is depicted on *Figure 2.10* with main specifications (*Table 2.2*). *Figure 2.11* shows the dimensions and a basic scheme of the electrical connections for the pressure sensor, whose electrical connection to the data acquisition hardware consists of only 2 wires, one for the positive terminal (1) and the other for the 0 V terminal (2).

Wika[®] *A-10* pressure sensors, in general, are designed for industrial applications such as hydraulics, pneumatics and automation, while ensuring a high environmental resistance to vibrations, shock, wide temperature variations, radio-frequency interference and other extreme conditions. They are made of austenitic stainless steel AISI 316L (low percentage of Carbon, high percentage of Chromium and Nickel)(wetted parts and case) which ensures a better durability and reliability over time. The specifications for this family of transducers are listed in the following table (*Table 3.1*).

Parameters	Values
Pressure Ranges	0..15 <i>psi</i> to 0..10000 <i>psi</i>
Signal Output	4-20 <i>mA</i> , 0-5 <i>V</i> , 0-10 <i>V</i> , others
Power Supply	8..30 <i>V(DC)</i> 14..30 <i>V(DC)</i>
Response Time	< 4 <i>ms</i>
Non-Linearity	$\leq 0.5\%$ BFSL, $\leq 0.25\%$ BFSL
Operating Temperature	273 to 353 <i>K</i> (0 to 80°C)
Materials	AISI 316L, silicone oil

Table 2.1: *Wika*[®] *A-10* pressure transducers specifications

2.2. Description of components



Figure 2.10: Wika[®] A-10 pressure transducer

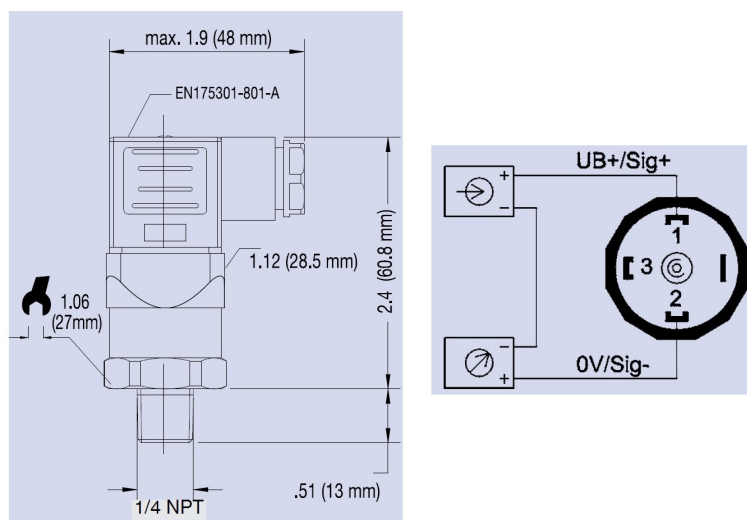


Figure 2.11: Dimensions and internal detail with electrical connections

Pressure Range	Output Signal	Power Supply
0...10 bar	4...20 mA	DC 8...30 V

Table 2.2: Pressure transducer main specifications

2.2.4 Microphone

The last type of sensor which is part of the tests facility is a microphone, whose aim was that of measuring pressure waves amplitude and frequency spectrum. A Logitech® Dialog-320 microphone (*Figure 2.12*) has been utilized during the test campaign, connecting it directly to the PC audio input port. This choice has been mostly driven by the peculiar frequencies of the periodical oscillations which were expected, from the previous experimental studies, to be included in the $0-10$ KHz range [8], as well as by reasons of simplicity. The microphone has been placed in the flow zone comprised between the nozzle exit and the resonator cavity inlet, in order to detect the pressure waves oscillations in that area.



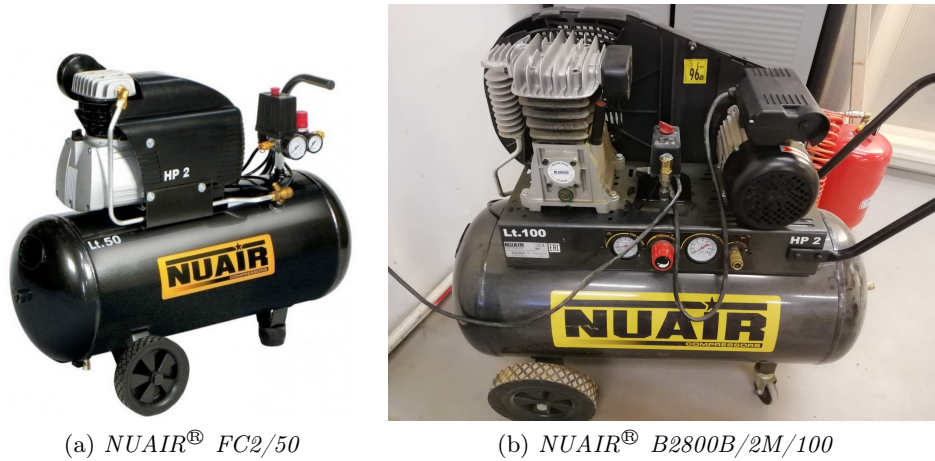
Figure 2.12: *Microphone used for amplitude and frequency measurements*

Sensitivity	Frequency Range	Input Impedance
-67 dB	100 – 16000 Hz	2000 Ω

Table 2.3: *Microphone main specifications*

2.2.5 Compressed air line

The gas flow needed to carry on the experimental tests has been provided by two different air compressors while, during the validation phase, an additional air tank has been used in order to have a more stable pressure level on the pneumatic line, as it will be seen on *Section 2.4.1 (Figure 2.27)*. The two compressors have some differences, in particular as concerns reservoir capacity and maximum deliverable pressure. However, both are equipped with manometers and at least one pressure regulator, for having a first simple reading of the air reservoir pressure and changing the output pressure level when required.



(a) NUAIR[®] FC2/50

(b) NUAIR[®] B2800B/2M/100

Figure 2.13: Compressors used on the experimental tests

The NUAIR[®] FC2/50 (*Figure 2.13, left*) is a light, reliable and lubricated single-stage coaxial air compressor which belongs to the company traditional range. It is particularly indicated for hobby workers, with its strong points being the efficient cooling method and the over-sized electric motor. It has been mostly used during the validation phase because of the high experimental nature of the latter, besides the uncertainties regarding the exact pressure level range necessary for the resonance heating phenomenon to occur. The NUAIR[®] B2800B/2M/100 (*Figure 2.13, right*) is a powerful single-stage, bycylindrical air compressor aimed at a more professional use for small businesses and craftsmen, thanks also to its large reservoir. It has substituted the previous compressor during the final upgrade phase because of its higher achievable pressure levels needed for reproducing the phenomenon being stud-

<i>Parameters</i>	FC2/50	B2800B/2M/100
Reservoir	50 L	100 L
Power	2 HP (1.5 kW)	2 HP (1.5 kW)
Max Pressure	8 bar (116 psi)	10 bar (145 psi)
Air Flow Rate	222 l/min	255 l/min
Speed	2850 rpm	1250 rpm
AC Power Source	230 V/50 Hz	230 V/50 Hz

Table 2.4: *Compressors main specifications*

ied, as understood from the previous experimental tests. Specifications for both compressors are showed on *Table 3.4*.

As mentioned at the beginning of this paragraph, a portable tank to store compressed air has been used during the first tests (*Figure 2.14*). It can store up to 14 litres of air, being equipped with a pressure gauge and a pressure regulator, and it can be connected to the compressed air line through bayonet and quick couplings.

Figure 2.14: *Compressed air tank*

2.3 Data acquisition and processing

2.3.1 Hardware section

The task to acquire data from the sensors previously described and after to process and show them in the form of graphics is assigned to data post-processing hardware. This consists of a data control and acquisition device from *National Instruments*[®] (*NI*) called *Compact Field Point*, which is organized in various modules connected to a common backplane with the latter, in turn, mounted on a holed metallic panel, as seen below on *Figure 2.15*. A simple scheme of the selected *NI*[®] *cFP-1804* dimensions and backplane connections is shown on *Figure 2.16*.

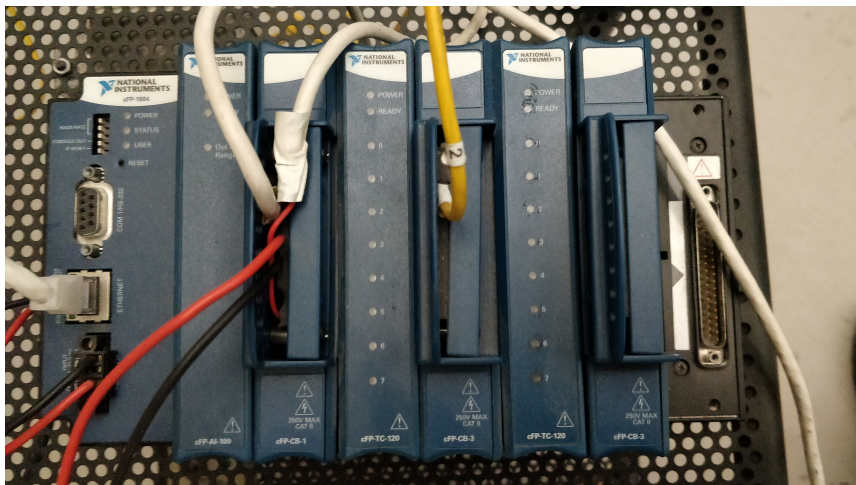


Figure 2.15: *NI Field Point modules*

It possesses 8 connector sockets organized in 4 slot groups in order to accommodate a maximum of 4 *I/O modules* with their respective *connector blocks*. Its main tasks are those of:

- interfacing the data acquisition system constituted by *I/O modules* with the data processing software and the PC, through a high speed ethernet or a serial (RS-232) network ;
- interfacing data acquisition modules with their connector blocks ;
- give electrical power to the *I/O modules*, while being connected to an external power supply .

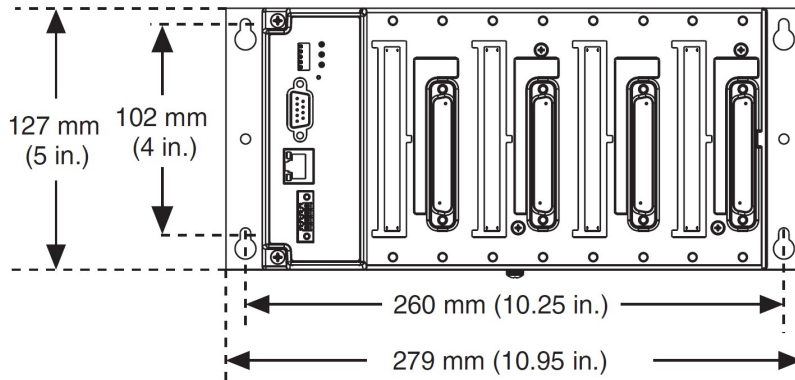


Figure 2.16: *Basic scheme and dimensions of NI[®] cFP-1804 with backplane slots*

It has been decided to use an ethernet connection because of the superior speed and stability, besides a negligible amount of data losses.

As regards the data acquisition, in general the signals from the sensors (thermocouple or pressure transducer) are directly received by the connector blocks to which they are physically connected with wires, before being sent to the acquisition modules. Two different types of I/O modules have been mounted on the backplane based on the data to be collected during the tests. The NI[®] *cFP-TC-120* has been used as a thermocouple input module, in order to measure the temperatures through the aforementioned K-type thermocouple. A scheme for the connection of a thermocouple to the TC-120 module is depicted on *Figure 2.17*, which refers to a shielded wiring thermocouple. Signals from the 8 channels are received by the module, in addition to that from the cold junction which allows the relative temperature signals to be translated into absolute temperature signals. A linearization and a cold-junction compensation are available for this module and for different types of thermocouples, including K-type, as well. Positive and negative leads of thermocouple must be connected respectively to *IN+* and *IN-* terminals, while an eventual shield should be connected to the *COM* terminal. All eight channels possess a *COM* terminal that connects them to an isolated common ground reference (indicated with *C* on *Figure 2.17*), besides being filtered, amplified and then sampled by a 16-bit ADC (analog-to-digital converter). Otherwise, for the pressure level measurements coming from the Wika[®] A-10 transducer a NI[®] *cFP-AI-100* has been uti-

Figure 2.18 shows the electrical diagram for the connection of a current source to the AI-100 module, which in this case is represented by the output signal coming from the pressure transducer.

The connector blocks used for the thermocouple and the pressure transducer modules are the *cFP-CB-x*, respectively *cFP-CB-3* and *cFP-CB-1*. Some differences exist between one another, but both have an operating temperature range comprised between -40 and 70 °C and are equipped with tie-wrap anchors to keep the wires in place. The sensors are directly wired to these modules, which act as a bridge between a sensor and its data acquisition (or I/O) module which elaborates the signal received. The *cFP-CB-3* connector block is connected to the thermocouple module *cFP-TC-120* and possesses 18 terminals, as depicted on Figure 2.19, which shows its connection screw-terminals which are related to its 8 channels. The *CB-3* module is more suitable for temperature measurements because of its isothermal construction which allows to minimize thermal gradients generated across the terminals due to heat dissipated by adjacent modules. This could bring, in fact, to accuracy errors between channels during the measurements. As concerns the thermocouple used for the experimental tests, it has been connected to the first channel (CH 0) thus to the screw-terminals 1 (IN+) and 2 (IN-), as it can be seen from Figure 2.19. The other connector block, used for pressure measurements, is the *cFP-CB-1* which has 36 terminals, as shown on Figure 2.20. It is designed for general-purpose as well as hazardous voltage operat-

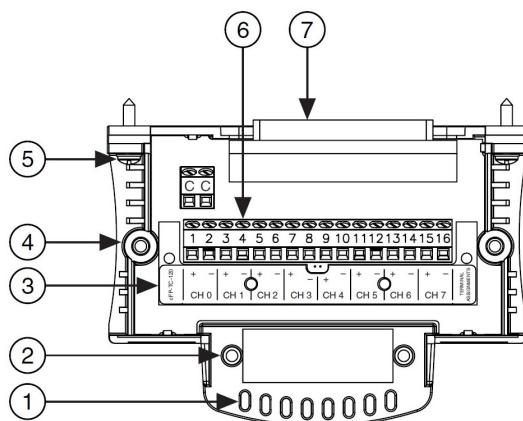


Figure 2.19: Internal screw-terminal arrangement for NI[®] *cFP-CB-3* connector block [1]

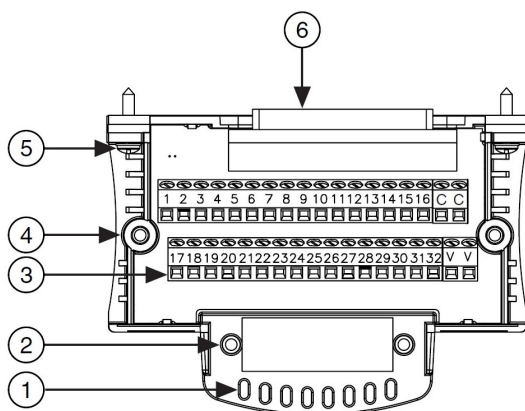


Figure 2.20: Internal screw-terminal arrangement for NI[®] cFP-CB-1 connector block [1]

ions with all various compact Field Point I/O modules. The electrical scheme drawing depicted below on *Figure 2.21* shows how the pressure transducer is connected to its connector block.

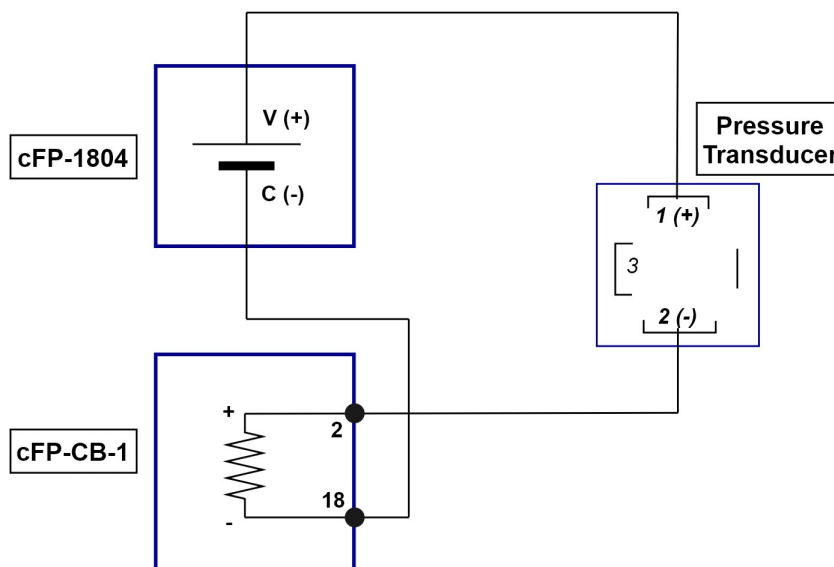


Figure 2.21: Pressure transducer and cFP modules electrical connection diagram

It can be also seen below, from the *Table 2.6*, that the first channel (CH 0) has been used in this case as well, in particular the current input terminal 2

because of the current output of the transducer and the common reference terminal 18.

Channel	V _{in}	I _{in}	V _{sup}	COM
0	<i>1</i>	2	<i>17</i>	18
<i>1</i>	<i>3</i>	<i>4</i>	<i>19</i>	<i>20</i>
...

Table 2.6: *cFP-AI-100 channels associated to cFP-CB-1 terminals* [2]

2.3.2 Software section

In order to process the signals received from the data acquisition hardware, the LabVIEW[®] development environment from NI[®] has been chosen. It is based on a visual programming language and mainly used for data acquisition, instrument control and in general for industrial applications. The scripts set up to perform the experimental tests on the resonator are based on the detection of different types of data:

- *Temperature*, through the thermocouple ;
- *Amplitude* and *Frequency spectrum*, through the microphone ;
- *Pressure level*, through the pressure transducer .

The data acquired from the various sensors can be visualized on graphics through specific blocks, as seen on the next figures of this section. After that they can be reported on an Excel[®] sheet by right-clicking on the graphic, examples of which will be seen on *Chapter 3*.

The first script shown below on *Figure 2.22* allows the cFP thermocouple module to acquire temperature data from the first and visualize them on a temperature-time graphic. The time has been set up to *1000 ms* because of the response time of the thermocouple which is in the order of seconds. The second script (*Figure 2.23*) is related to the measurement of the pressure waves amplitude and the visualization of their frequency spectrum through the microphone. The block *Data* gives the wave amplitude graphic as a function of time, while the *waveform graph* block provides an amplitude-frequency graphic related to the resonance phenomenon occurring upstream and inside the cavity.

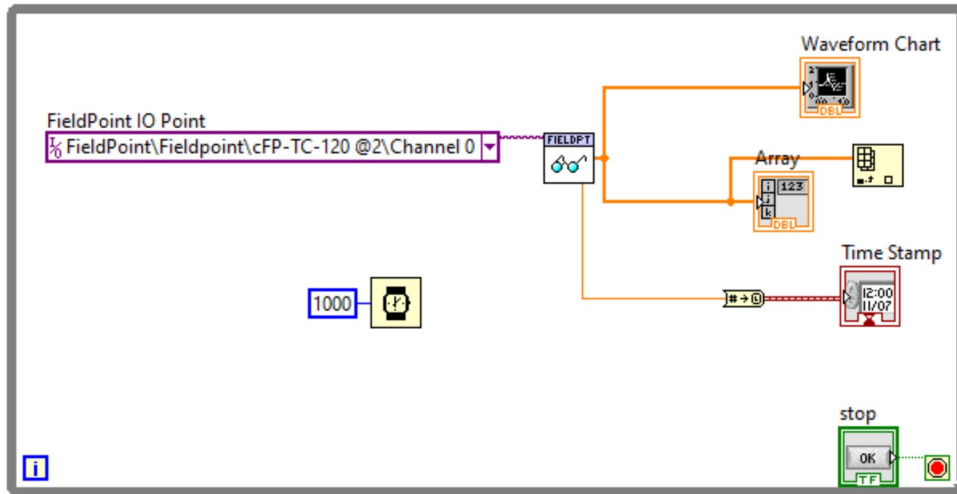


Figure 2.22: LabVIEW[®] script used for acquisition and processing of temperature signals from the thermocouple

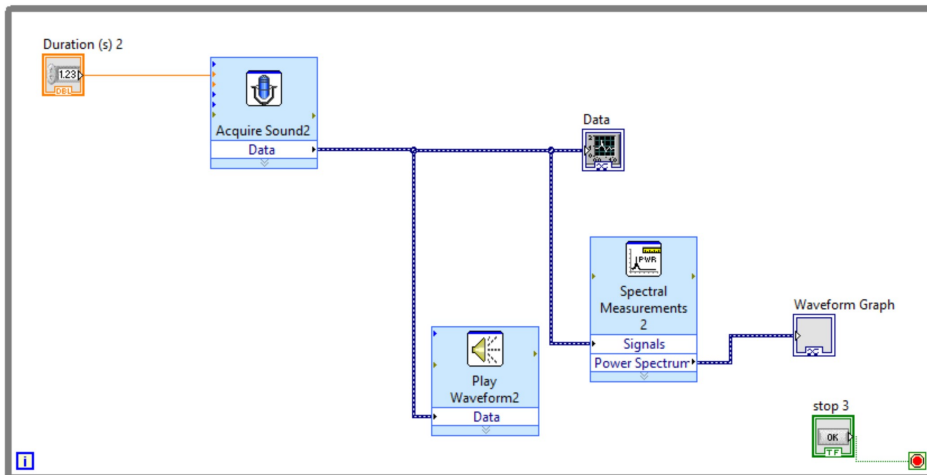


Figure 2.23: LabVIEW[®] script used for acquisition and processing of pressure waves amplitude and frequency signals from the microphone

Both the scripts just shown have served during the validation phase, while that for pressure measurements has been implemented during the subsequent phase when the entire facility has been improved. This last script is depicted on Figure 2.24. It shows, in this case, an additional "if" case block which has been used to calibrate the pressure transducer. While changing from *TRUE* to *FALSE* the user respectively enables or disables the direct reading

2.3. Data acquisition and processing

of the pressure level from the cFP module. The three scripts just described have been implemented in a single script in order to have a simultaneous measurements of the parameters needed to be acquired for each test.

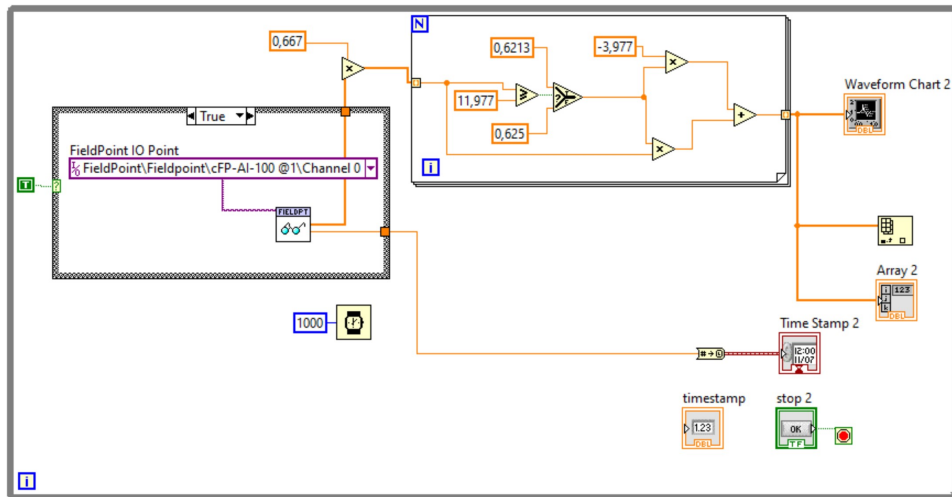


Figure 2.24: LabVIEW[®] script used for acquisition and processing of pressure levels read by pressure transducer

2.4 Global facility setup

In this section an overview of the entire facility is shown highlighting and motivating the subsequent steps and improvements made to build it, from the initial tests to the final configuration.

2.4.1 Initial tests setup

The initial part of validation phase of this experimental study had the only purpose to create the proper pressure and geometrical conditions for the resonance heating phenomenon to occur. The first apparatus thus assembled represents a very basic configuration as concerns the resonator, which has been obtained by using a block of wood, and then cutting in it the cavity needed for the tests (*Figure 2.27*). The *3-step* configuration has been used for the wooden resonator, with the dimensions shown on *Figure 2.26*. The block has been fixed to a holed panel through two screws from the bottom-up, and the thermocouple placed on the rear side of it. However, the three holes constituting the cavity were slightly disaligned due to manufacturing errors and the resonator internal walls were not so smooth. In addition, pressure drops on the initial pressure line have been detected, due to the presence of many junctions. These have been, therefore, the main causes of the lack of significant results during the first validation tests, together with the lower power of the compressor.

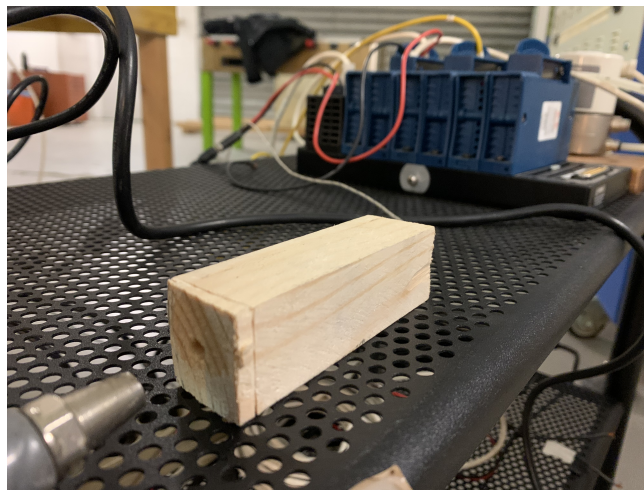


Figure 2.25: Wood block with cavity hole used for first validation tests

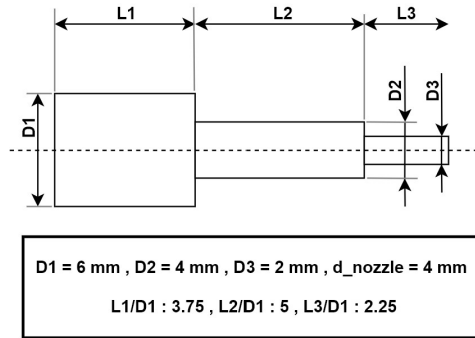


Figure 2.26: Wood 3-step cavity dimensions

As regards the compressed air line, initially an extendable compressor tube (the orange tube visible on *Figure 2.27*) with its terminal nozzle has been adopted in order to create the air flow, and the *NUAIR[®] FC2/50* compressor (described before on *Section 2.2.5*) has been used as air supply. Subsequently, after observing the inability for the compressor to maintain a stable pressure level, because of its limitations regarding the maximum effective deliverable pressure, it has been decided to use an additional air tank. The tank has been placed after the compressor, trying to establish an air flow with the least possible pressure oscillations (*Figure 2.27*). Together with this modification, it has been chosen to use another material for the resonator. Hence, a cavity has been obtained from a cylinder of *PMMA* with the same internal 3-step configuration and dimensions, as previously described on *Section 2.2.1*. For the latter, the same inaccuracies of the wood resonator have been identified, with a visible disalignment due to manufacturing difficulties, being *PMMA* harder than wood. Resonator and nozzle coupled together can be observed below on *Figure 2.28*. As seen from the figure, the two components have been fixed to a table by means of screws, nuts, plus some metal sticks and hose clamps to have an enough fixing of the system, and obviously to withstand pressure and recoil forces acting on the latter. The thermocouple is inserted from the resonance tube side at cavity endwall, to be less invasive. The *Figure 2.29* shows a basic scheme of the connections between the single components of the facility, with the dashed area comprised between nozzle exit and resonator inlet where the microphone has been placed.



Figure 2.27: Compressor and tank set up for validation tests

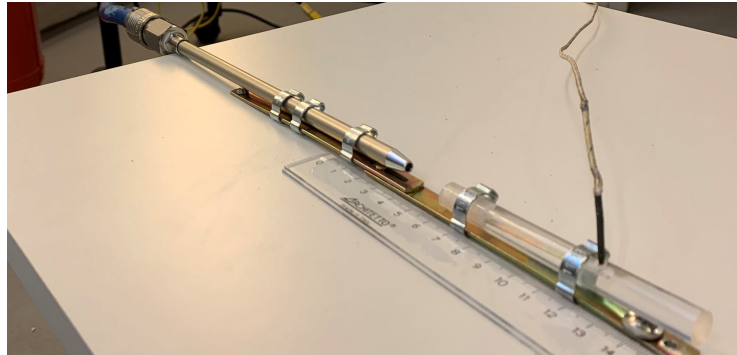


Figure 2.28: Nozzle and PMMA resonator configuration for validation tests

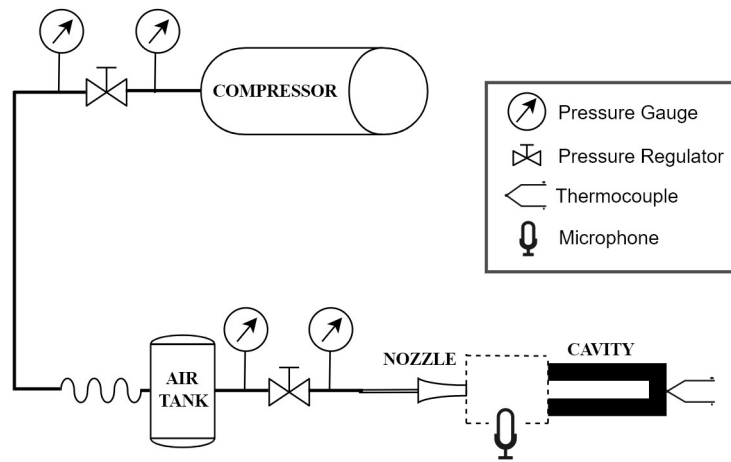


Figure 2.29: Scheme of validation tests facility

2.4.2 Final facility setup

The next step done after having performed the validation tests and verified the resonance heating process occurring at PMMA cavity base, the aim of the experimental work shifted onto an improvement of the total facility. In fact, some components have been added while some others have been set aside or modified. First of all, another compressor has been utilized in order to have a higher maximum deliverable pressure (the *NUAIR*[®] *B2800B/2M/100* described on *Section 2.2.5*, with a pressure limit of *10 bar*) and so being able to work with higher and more stable operating pressure levels, as discussed on the previous paragraph. Therefore, in this facility upgrade phase the air tank has not been used anymore. This upgrade has involved the resonator configuration, as well. As shown on *Figure 2.30*, the conical resonator made through additive manufacturing described on *Section 2.2.1* has been used.

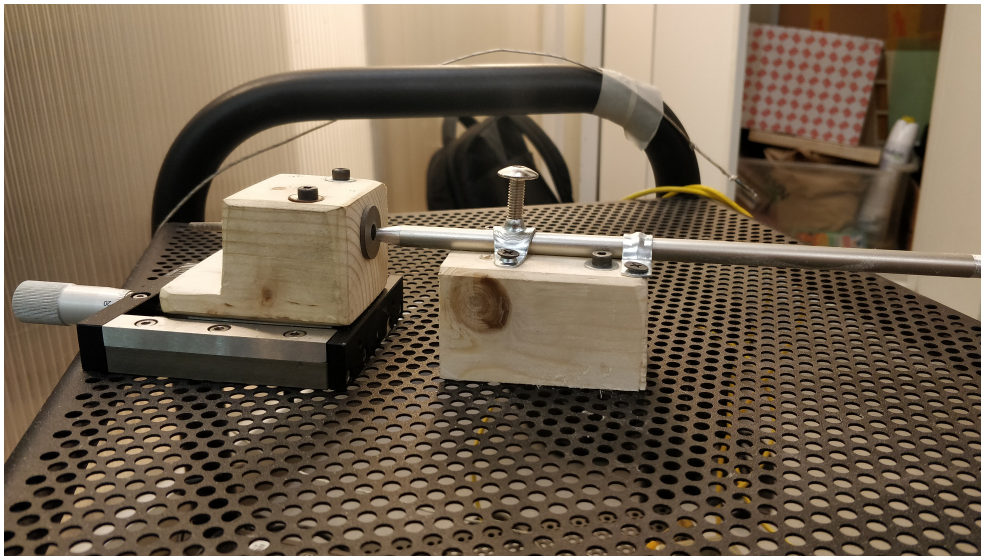


Figure 2.30: *Final facility configuration*

It has been inserted into a wood block designed on purpose to accommodate the new resonator, while holding it steady and aligning it with the nozzle. Moreover, a *micrometric positioning sliding plate* has been added to the facility in order to enable the resonator embedded into the wood block to change its horizontal position with a high precision. A detailed picture of the sliding plate is depicted on *Figure 2.31*. The nozzle has also been fixed to another wood block through some hose clamps and screws, and aligned with

the cavity along both vertical and panel plane lateral axes. The sliding and the wood pieces have been attached to the holed panel as done previously during the validation phase.

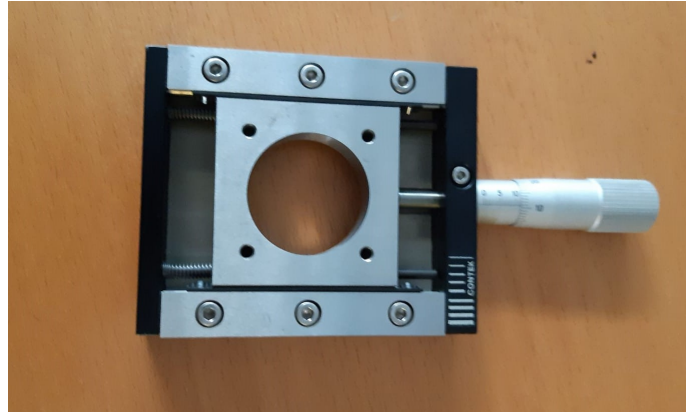


Figure 2.31: *Micrometric positioning sliding*

The last improvement made during this phase has been that of adding a pressure transducer (*Wika[®] A-10*, described on *Section 2.2.3*) shortly before the nozzle. Hence, it has been possible to have a more precise measurement of the pressure upstream of the air flow. The scheme for the facility thus improved is shown below on *Figure 2.32*. As it can be seen, it is characterized by a higher grade of precision after the correction of some inaccuracies from the previous experimental apparatus.

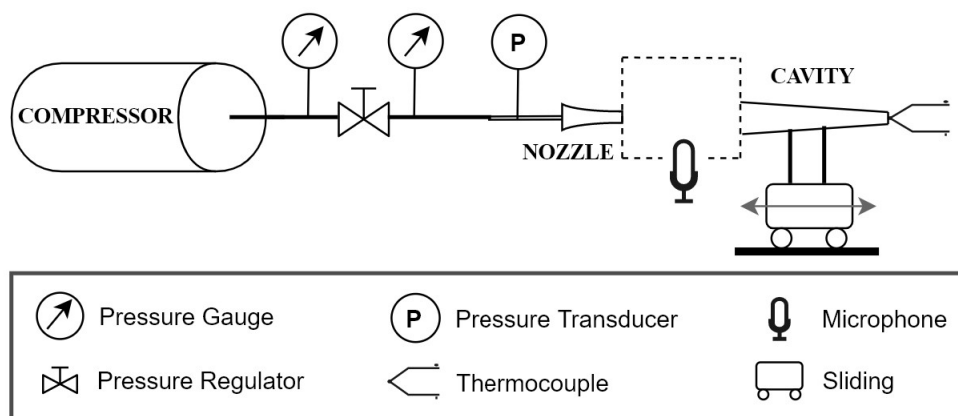


Figure 2.32: *Scheme of upgraded facility*

Chapter 3

Test Campaign

3.1 First validation tests

The experimental tests carried out have focused on reproducing, and therefore validating, the resonance heating phenomenon predicted to take place at the endwall of the resonator cavity as largely described on *Chapter 1*. The first tests conducted during the validation phase, which have been done using the *wood resonator* mentioned on the previous sections, have not given any significant results in terms of temperature increase inside the cavity.

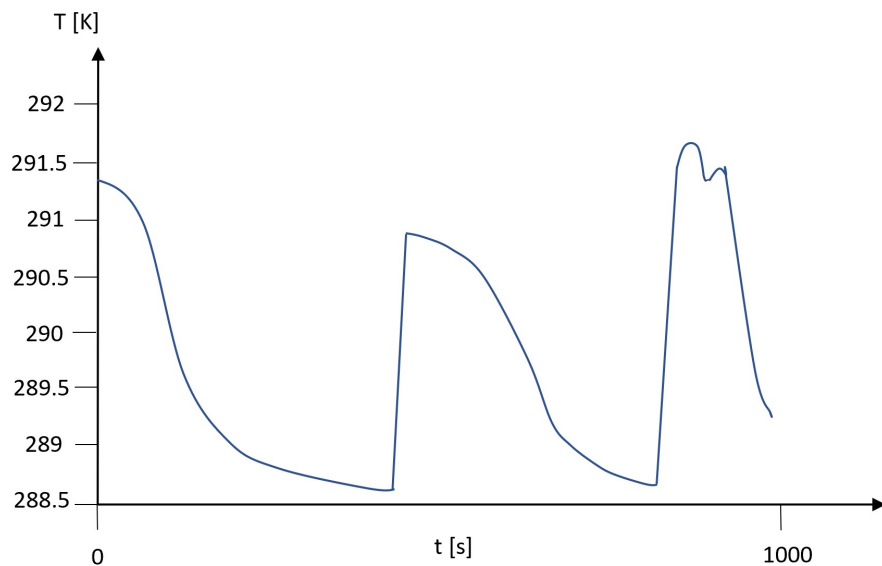


Figure 3.1: *Experimental test example performed with wood cavity*

In fact, as it can be seen from the test example of *Figure 3.1* the increase in temperature in respect to ambient pressure was negligible (about 3 K on this example). The reason of this has to be searched on the manufacturing imprecisions, as discussed before on *Section 2.4.1*. From there on the PMMA resonator has been chosen in order to perform the following tests, the results of which will be shown throughout this chapter. The *Table 3.1* below shows the first results obtained during the same series of tests and after carried out this modification on the cavity. They have been conducted with an operating pressure upstream of the nozzle about $p=5\text{ bar}$ for different values of s/d ratio (as defined on *Section 1.6.2*) with a fixed nozzle diameter $d=4\text{ mm}$ and hence a variable nozzle-cavity gap. As shown from the table below, the best result has been obtained from the third tests of the series, with an increase of 15 K from the ambient temperature. However, the pressure level was decreasing as the tests were running out, so it has not been possible to define a precise operating pressure. This problem has been faced during all the test campaign and partially solved with the help of the air tank, as described before on *Section 2.4.1*. The cause is due to the proximity of the operating pressure levels needed to trigger the phenomenon with the maximum effective pressure deliverable by the compressor (in this case, about 7.2 bar , with a limit of 8 bar indicated on the *NUAIR[®] FC2/50 datasheet*). As regards the detection of temperature the thermocouple has been placed on the side of PMMA resonator, at cavity base, avoiding the introduction of external disturbances in order to obtain reasonably accurate measurements.

TEST	1	2	3	4
s/d	6.25	3.75	2	0.75
T_{amb} [K]	290	290	290	290
T_{peak} [K]	300	303	305	293
ΔT [K]	10	13	15	3

Table 3.1: *First test series results with PMMA resonator*

The second series of experimental tests performed have given better results than the first after increasing pressure level to 7 bar but, at the same time,

increasing the descent rate of the pressure inside the compressor air reservoir. Despite this last inconvenience, it can be seen from the *Table 3.2* the increase of the maximum temperature detected at cavity endwall. For these tests the s/d ratio has been kept near the value of 2, considering the best results obtained on the previous series, which have been in fact confirmed with a higher pressure level, as well. Moreover, a fairly strong whistle related to the pressure waves oscillations has been recorded attesting the actual occurrence of the resonance heating phenomenon inside the cavity. The peaks of temperature related to the resonance heating at the cavity base is shown below on *Figure 3.2*.

TEST	1	2
s/d	2	3
T_{amb} [K]	290	290
T_{peak} [K]	350	340
ΔT [K]	60	50

Table 3.2: *Second test series results with PMMA resonator*

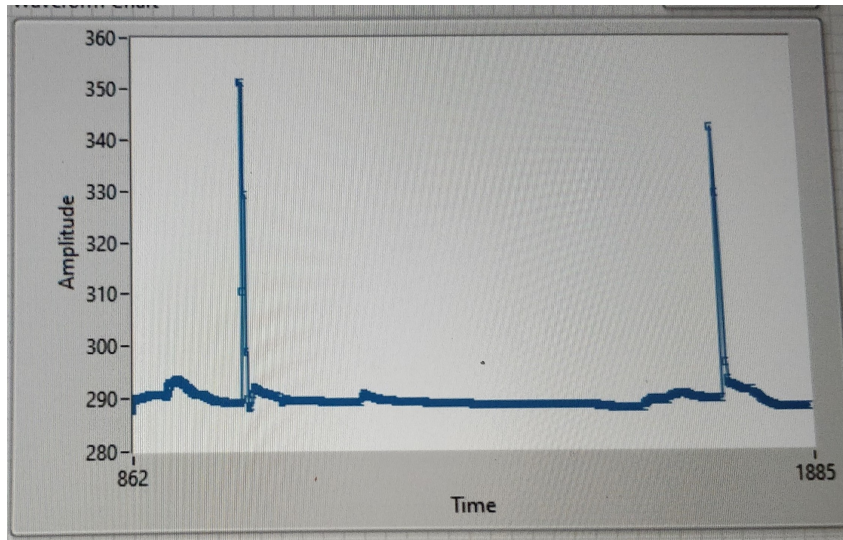


Figure 3.2: *Second tests series temperature graphic*

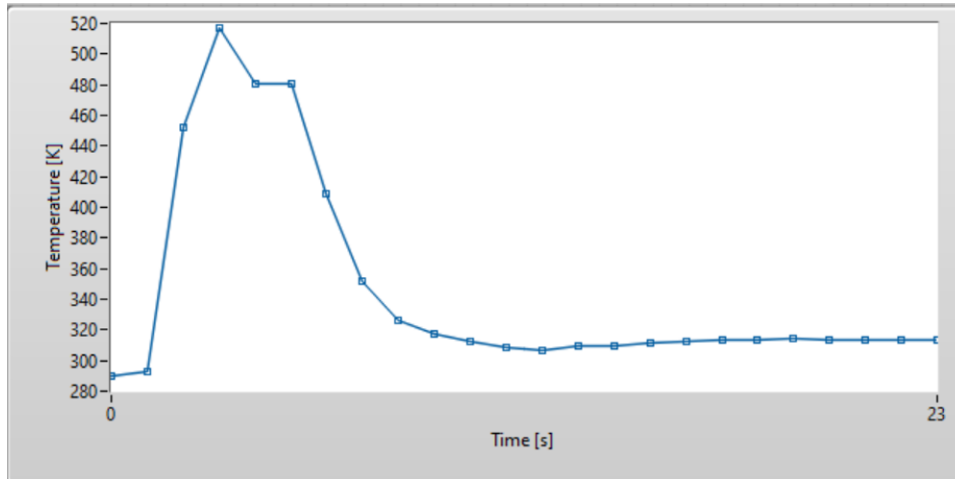
3.2 Final validation tests

After this first part of the tests campaign, it has been observed that pressure levels were not enough to reproduce the phenomenon. However, the inaccuracies of the cavity geometrical dimensions and the disalignment between the latter and the nozzle have also adversely affected the results. In addition, the thermocouple shows a delay in its detecting time, between the exact moment on which the temperature rises up and when the electric signal arrives to the data acquisition hardware. This delay, estimated being about 2-3 seconds, could have caused further inaccuracies on temperature measurements taking into account the typical time of the phenomenon which is attested to be in the order of some *milliseconds*. Therefore, it has been decided to make some upgrades as concerned the compressed air line, while trying to solve the issues related to the significant pressure oscillations. It has been understood that a more powerful compressor (with a power of about 4 HP) was needed in order to rise the pressure limit, moving away the operating pressure range from the latter. It has been figured out the air consumption to be excessive for carrying on the experimental tests with a maximum pressure as high as 7 bar without having significant pressure decreasing. The latter is due to the inability for the compressor used to maintain the desired pressure level compared to such high air flow rate required from the system. The air flow rate should be less than 140 l/min to keep a stable pressure level of 7 bar. Besides this, the manometers were not so reliable in terms of measurement accuracy so the need of a more precise pressure sensor has been found out. In fact, this improvement has been made after the end of validation tests, in the upgrade phase described on *Section 2.4.2*. An air tank has been thus added to the facility in this second part of the tests, as also discussed previously on *Section 2.4.1*.

In order to perform the next tests series after this modification, a pressure of 7 bar upstream of the nozzle and a constant $s/d = 1.75$ have been maintained, having fixed both nozzle diameter (4 mm) and also nozzle-cavity distance 7 mm. These tests have produced the results shown below on *Table 3.3*. As it can be observed on these final tests it has been reached the highest temperature at the cavity base (520 K = 793 °C) considering all the validation phase. This temperature peak can be seen from *Figure 3.3*, which also shows the delay of the detection due to the thermocouple. For this tests

phase the thermocouple has been initially kept in place manually on the side of the PMMA resonator (as said on the previous paragraph), while after it has been attached with a specific glue to the latter. The last choice has been done after observing some air leakages occurring through the hole where the temperature sensor was inserted. Considerable differences between the single tests of this phase could be seen though from the table below, even while keeping fixed the nozzle-cavity gap and the pressure. This high degree of variation is mainly due to the still slight roughness of the experimental apparatus, easily influenced by external disturbances.

TEST	1	2	3	4
Amplitude	2.7×10^{-4}	5×10^{-4}	1.5×10^{-4}	1.8×10^{-4}
f_{peak} [kHz]	3.8	3.8	3.8	3.8
T_{amb} [K]	290	290	290	290
T_{peak} [K]	470	340	520	350
ΔT [K]	180	50	230	60

Table 3.3: *Final validation tests results*Figure 3.3: *Maximum temperature reached during final validation tests (Test #3)*

Frequency and amplitude of pressure waves oscillations related to the same previous test have been acquired through the microphone and reported on the graphic, as seen below from *Figure 3.4*. Apart from the frequency peak of 3.8 kHz , other two of them with a lower amplitude can be seen from the figure, which are those at about 1.7 kHz and 7.7 kHz .

It can be noticed that one of the previous frequencies (about 1.7 kHz) is about the same of the main frequency recorded by TUM during their experimental tests on 2014 (about 1.96 kHz) [8]. A high amplitude screeching noise has also been recorded this time, especially at the beginning of each single test which decreased its amplitude when the pressure decreased. This could represent a shifting between the two different operating mode of the resonator, from the jet screech to the jet regurgitant mode. However, it should be said that the detection of the pressure waves oscillations noise could have been influenced by environmental acoustic disturbances, although at quite low level.

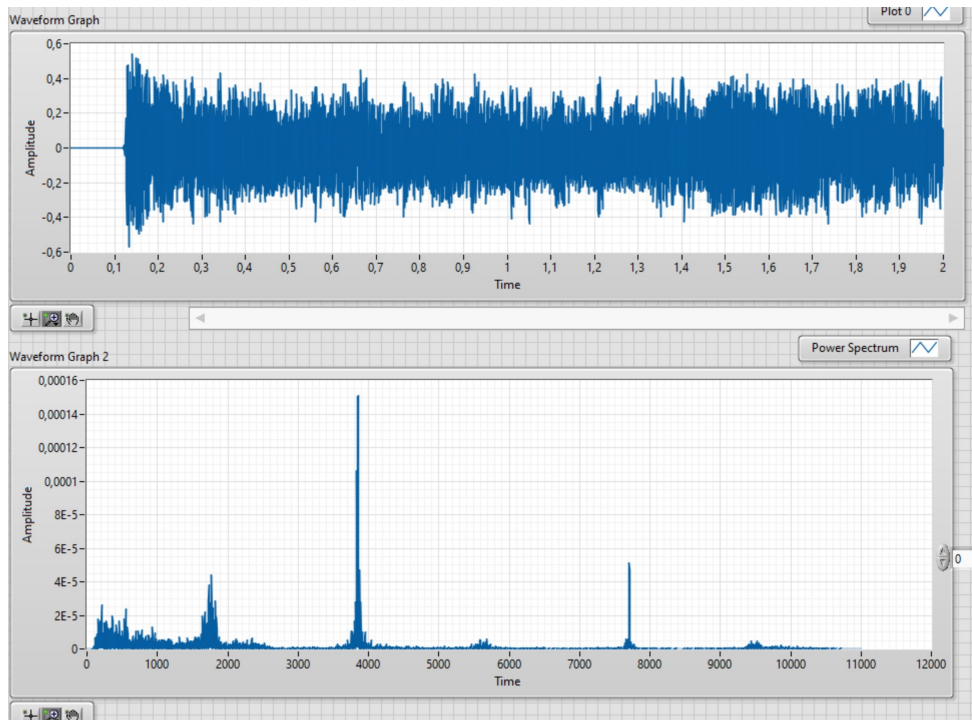


Figure 3.4: *Pressure waves amplitude and frequency spectrum corresponding to the test #3*

Amplitude and frequency spectrum related to the first two tests of the final validation phase (*test #1, #2 of Table 3.3*) have been reported on graphics, as well, as it can be seen from the following *Figure 3.5* and *Figure 3.6*. In general, the frequency spectrum refers to the entire time history, hence with the presence a variable NPR. This means that an overlapping of the different operating modes (JRM, JSM) could have occurred. After a first look to the frequency spectrum, it can be said that the most amplified frequencies of the resonance oscillations remains that in the order of 3.8 kHz which fairly decreases until about 3.6 kHz when the cavity endwall temperature decreases. As regards the frequencies less amplified than the previous one, the peak corresponding to the frequency of 1.7 kHz occurs only on the maximum temperature case, while on the cases depicted below with lower temperatures is not visible. On the contrary, the peak at 7.7 kHz becomes to be visible even at temperature closer to that of ambient, and fairly increases its level of amplitude while the temperature increases. Some peaks can be visible in a frequency range of about $200\text{-}600\text{ Hz}$, in a more pronounced way for temperatures lower than 520 K . This last peak decreases in amplitude when the temperature rises instead, as seen from the first frequency spectrum graphic on *Figure 3.4*. On the latter, two other peaks appear in the frequency ranges of $5.5\text{-}5.7\text{ kHz}$ and $9.4\text{-}9.6\text{ kHz}$, but they are barely visible because very low in amplitude.

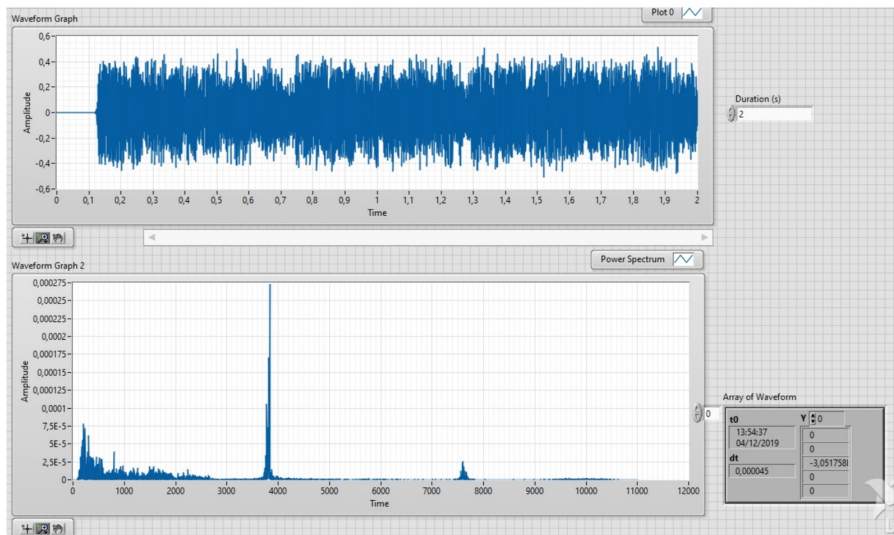


Figure 3.5: *Pressure waves amplitude and frequency spectrum for test #1*

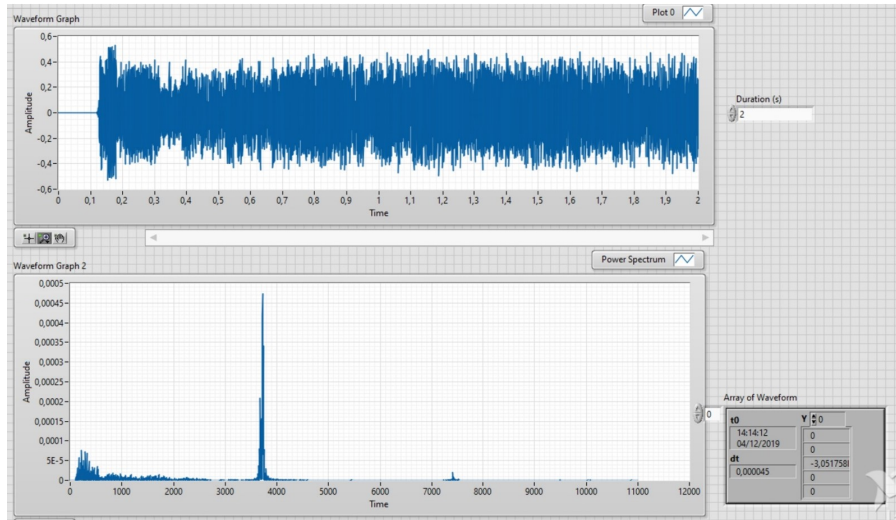


Figure 3.6: Pressure waves amplitude and frequency spectrum for test #2

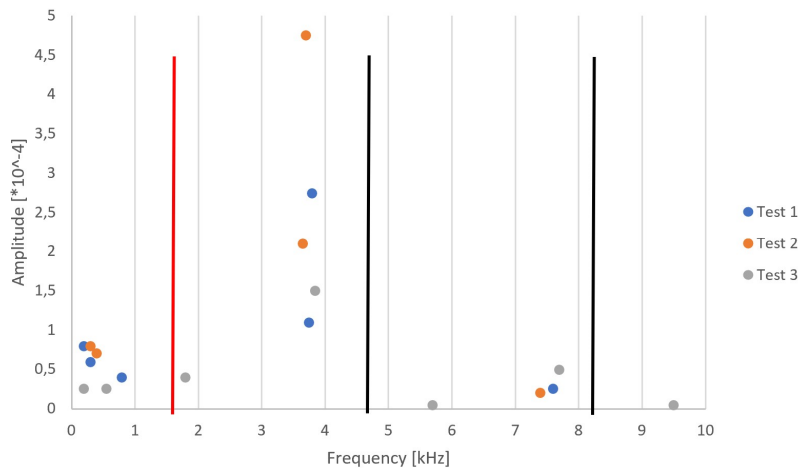


Figure 3.7: Frequency spectrum and amplitude of tests #1, #2, #3, with first three resonator cavity longitudinal frequencies

The results regarding the frequency spectrum of all three tests are depicted on the graphic below (*Figure 3.7*). The vertical lines indicate the three main longitudinal frequencies associated with the pressure oscillations for the first three tests conducted on *Table 3.3*, according to the different colours indicated on the right side of the figure. As it can be observed from the graphic, the first three longitudinal are indicated, in particular the *first longitudinal* in red and the *second* and *third longitudinal* in black. These natural fre-

quencies have been calculated as follows, from the one-dimensional acoustic theory [14]:

$$f = (2n - 1) \frac{a}{4L} \quad , \text{with } n=1,2,3,..$$

where a is the speed of sound, having considered in this case an ambient temperature of about $15 \text{ }^\circ\text{C}$ (about 341 m/s), while L represents the PMMA cavity length (51.5 mm). The following natural longitudinal frequencies (L_1 , L_2 , L_3) have been therefore calculated:

$$L_1 = \frac{a}{4L} = 1.655 \text{ kHz} \quad n = 1$$

$$L_2 = 3 \frac{a}{4L} = 4.695 \text{ kHz} \quad n = 2$$

$$L_3 = 5 \frac{a}{4L} = 8.275 \text{ kHz} \quad n = 3$$

Moreover, it has been observed from numerical simulation conducted by Chang and Lee [14], that the regurgitant frequency is really similar to the main longitudinal frequency predicted by the one-dimensional acoustic theory. The exact value of the first differs from the latter because of the influence of the streamline deflection ahead of the resonance tube. However, the variation of the tube length influences as well the correspondence between the acoustic theory and the numerical simulations [14].

Chapter 4

Conclusions

4.1 Discussion of results

The main objective of this experimental work was that of reproducing the resonance heating phenomenon and validating it, and it has been actually achieved. A relevant peak of temperature has been recorded, demonstrating that the developed experimental setup is suitable to reproduce the phenomena under investigation. Some dominant oscillations frequencies in terms of amplitude have been also found, besides recording noises related to the establishment of the different resonator operating modes. Generally, the results obtained are in accordance with the expectations as well as with scientific literature regarding the phenomenon. Some attempts have been done before obtaining relevant results in terms of increase of temperature, mainly because of the roughness of the apparatus which has been improved after the tests phase.

The upgrade of the facility was, in fact, the second objective of the present study as much important as the validation tests. Through this phase some critical issues have been solved. First, with the help of a new and more powerful compressor to be able to maintain a stabilized pressure during the experimental tests. In addition, the pressure transducer introduced right upstream of the nozzle and the micrometric positioning sliding plate have provided respectively more precise pressure measurement and distance regulation between the nozzle and the resonator. It is worth mentioning the wood blocks and the holed panel used for fixing nozzle and resonator, as well, which have substituted the hose clamps and metal sticks eliminating

some inaccuracies from the test facility.

An additional test campaign with the upgraded test facility was planned, but it has been cancelled because of the unexpectedly critical situation occurred, due to COVID-19 pandemic global emergency.

4.2 Future perspectives

The next and natural step to make in order to obtain more reliable and precise results is that of carrying on with the improvement of the experimental apparatus already built up. The new conical metallic resonator designed starting from a 3-D model and mounted on the upgraded facility has been inspired by the previous studies conducted on this topic. After this improvement, an eventual comparison with results obtained by TUM could be done. In addition, a vacuum chamber could be added to surround the resonator. This particular solution has been adopted by TUM in order to limit the heat losses through the external walls of the resonance tube [8], as described on *Section 2.1*.

Future tests will be conducted on a more improved facility with a higher level of precision, considering to use a more stable method to fix nozzle and resonator as well. The introduction of wood blocks has been demonstrated to be a better alternative than the previous fixing solution used during the validation tests phase. However, an "ad-hoc" support structure should be considered to be adopted in the future.

The experimental tests to be carried on in the next phase should examine in a deeper way the influence of the various parameters on the resonance heating process. In this experimental work, in fact, only a validation of the phenomenon has been performed even if the gathered results helped in broadly characterizing the phenomenon. Thanks to the micrometric positioning sliding plate, for example, the effect of nozzle-cavity distance will be studied in a more precise way as well. A possible improvement could be that connected to the installation of a schlieren or shadowgraph system in order to visualize the air flow coming out from the nozzle which enters the cavity. Such an additional device will help to understand more clearly the fluid dynamics features of the gas flow and how the latter affects the resonance igniter performances.

In general, efforts have to be made in order to better define how resonance

heating occur, by outlining how each parameter affects the latter. After carrying on more accurate tests, the following step could be that of considering the experimental apparatus also as part of an ignition system, and so focusing on the more practical applications of it. However, before reaching this phase a more detailed validation of the resonance igniter system should be done.

Bibliography

- [1] *Field PointTM Operating Instructions ,cFP-CB-1 and cFP-CB-3*, <https://www.ni.com/manuals/i/>.
- [2] *Field PointTM Operating Instructions ,FP-AI-100 and cFP-AI-100*, <https://www.ni.com/manuals/i/>.
- [3] *Field PointTM Operating Instructions ,FP-TC-120 and cFP-TC-120*, <https://www.ni.com/manuals/i/>.
- [4] B. Afzali and H. Karimi. Numerical investigation on thermo-acoustic effects and flow characteristics in semi-conical hartmann-sprenger resonance tube. *Proceedings of the Institution of Mechanical Engineers, Part G: Journal of Aerospace Engineering*, 231(14):2706–2722, 2017.
- [5] M. Albertini, E. Brocher, and C. Maresca. Influence of the nature of the gas on the thermal effects in a hartmann-sprenger tube(gas nature effect on wall temperature and heat transfer in hartmann-sprenger tube). 1971.
- [6] J.D. Anderson. *Modern compressible flow: with historical perspective*, volume 12. McGraw-Hill New York, 1990.
- [7] C. Bauer, P. Lungu, and O.J. Haidn. Numerical investigation of a resonance ignition system. In *8th European Conference for Aeronautics and Space Sciences*, 2019.
- [8] C. Bauer, J. Pauw, and O.J. Haidn. Numerical and experimental investigations on resonance ignition. In *Space Propulsion Conference*, 2014.
- [9] E. Brocher and J.P. Ardissonne. Heating characteristics of a new type of hartmann-sprenger tube. *International journal of Heat and fluid flow*, 4(2):97–102, 1983.

-
- [10] E. Brocher and C. Maresca. Mécanisme des échanges thermiques dans un tube de résonance. *CR Acad. Sci.*, 271:737–740, 1970.
- [11] E. Brocher and C. Maresca. Approximate calculation of heat transfer and longitudinal distribution of temperature at mouth of hartmann-sprenger tube. *Comptes Rendus Hebdomadaires des seances de l'Academie des Sciences Serie A*, 274(19):1425, 1972.
- [12] E. Brocher and C. Maresca. Etude des phenomenes thermiques dans un tube de hartmann-sprenger. *International Journal of Heat and Mass Transfer*, 16(3):529–538, 1973.
- [13] B.J. Cantwell. Fundamentals of compressible flow, 1996.
- [14] S-M Chang and S Lee. On the jet regurgitant mode of a resonant tube. *Journal of Sound and Vibration*, 246(4):567–581, 2001.
- [15] A. Conte, A. Ferrero, and D. Pastrone. Preliminary study of a resonant igniter for rocket engines. 2019.
- [16] A. Conte, J. Rabinovitch, E. Jens, A. Chandler Karp, B. Nakazono, and D. Vaughan. Design, modeling and testing of a O₂/CH₄ igniter for a hybrid rocket motor. In *2018 Fluid Dynamics Conference*, page 3239, 2018.
- [17] A. Dancelme, J. Shvab, A. Usbek, and P. Lungu. Investigation of characteristics of a resonance igniter. Technical report, TUM, 2018.
- [18] J. Danton, F. Villas Boas, K. Kessaev, and M. Niwa. Some peculiarities of resonance tube gas-dynamical heating. In *ENCIT 2000, Brazilian Congress of Thermal and Engineering Sciences*, 2000.
- [19] Yu B. Eliseev and A. Ya Cherkez. On the effect of an increase in stagnation temperature during gas flow over deep cavities. *Izv. Akad. Nauk SSSR, Mekh. Zhidk. Gaza*, (3), 1971.
- [20] J. Hartmann. On a new method for the generation of sound-waves. *Physical Review*, 20(6):719, 1922.
- [21] <https://www.ni.com/it-it/innovations/white-papers/16/temperature-sensor-basics.html>. Temperature sensor basics. Technical report.

- [22] M. Kawahashi and M. Suzuki. Thermal effects in a hartmann-sprenger tube. *Bulletin of JSME*, 22(167):685–692, 1979.
- [23] K.V. Kesaev. Theoretical model of a resonance tube. *Izvestiya Vysshikh Uchebnykh Zavedenii Aviatsionaya Tekhnika*, (2):49–52, 1990.
- [24] K. Kessaev, R. Vidal, and M. Niwa. Gas jet heat release inside a cylindrical cavity. *International Journal of Heat and Mass Transfer*, 46(10):1873–1878, 2003.
- [25] V.M. Kuptsov, S.I. Ostroukhova, and K.N. Filippov. Pressure fluctuations and heating of a gas by the inflow of a supersonic jet into a cylindrical cavity. *Fluid Dynamics*, 12(5):728–733, 1977.
- [26] R.F. McAlevy III and A. Pavlak. Tapered resonance tubes-some experiments. *AIAA Journal*, 8(3):571–572, 1970.
- [27] BR Phillips and AJ Pavli. Resonance tube ignition of hydrogen-oxygen mixtures. 1971.
- [28] V. Sarohia and L.H. Back. Experimental investigation of flow and heating in a resonance tube. *Journal of Fluid Mechanics*, 94(4):649–672, 1979.
- [29] V. Sarohia, L.H. Back, E.J. Roschke, and S.P. Pathasarathy. An experimental investigation of fluid flow and heating in various resonance tube modes. 1976.
- [30] M. Scervini. Thermoelectric materials for thermocouples. *Department of Material Science and Metallurgy, University of Cambridge, Cambridge*, 2009.
- [31] H. Sprenger. About thermal effects in resonance tubes. *News from the Institute of Aerodynamics at the ETH Zurich*, 21:18, 1954.
- [32] G.J. Sreejith, S. Narayanan, T.J.S. Jothi, and K. Srinivasan. Studies on conical and cylindrical resonators. *Applied Acoustics*, 69(12):1161–1175, 2008.

Acknowledgements

I would first like to thank Fablab Torino for their important technical support and their great availability given to perform this experimental work. Many thanks have to be done for Technische Universität of München (TUM) which has provided our workteam with the configurations for the experimental facility, in particular for the resonator, giving us in fact the first inspiration in carrying on this work.

I would like to thank, as well, Prof. Sara Biamino and Ing. Giulio Marchese of the Department for Applied Sciences and Technologies (DISAT) of Politecnico di Torino for the production of the final experimental configuration of the resonator used for tests. Also thanks to Ing. Massimiliano Mattone for having provided the team with the micrometric positioning sliding plate, essential for the upgrade of the experimental facility.

Finally, thanks have to be addressed to Prof. Dario Pastrone for the chance given to me in working into this experimental project, to Ing. Antonietta Conte for her precious advices having worked alongside me especially on the first phases of this thesis work, to Prof. Luigi Spagnolo for essential help given on data post-processing software and hardware, as well as to all teamwork members for their significant support.